THE CORRELATED SPECTRAL FUNCTION OF THE NUCLEUS

INAUGURAL-DISSERTATION

zur
Erlangung der Würde eines Doktors der Philosophie
vorgelegt der
Philosophisch-Naturwissenschaftlichen Fakultät
der Universität Basel

von

Christophe Normand

aus Bordeaux (France)

Basel 2004

Genehmigt von der Philosophisch-Naturwissenschaftlichen Fakultät auf Antrag von Professor Dr. I. Sick und PD Dr. J. Jourdan.

Basel, den 21. Oktober 2004

Prof. Dr. H.J. Wirz
Dekan

Acknowledgements

Concerning this work, a lot of people were involved in its experimental part in Jefferson Lab or in the analysis of the data at the Physik Institüt in Basel. I am indebted to most of them for managing this thesis.

First, I would like to thank my supervisors Ingo Sick and Jürg Jourdan for their help and their support over these last years. It was a great opportunity to work with two wise physicists in a challenging and exciting environment. Their sagacity in physics or experimental work and their nature were a strength in the understanding of the curious microcosmos of nuclear physics.

Next, I want to thank Daniela Rohe; her commitment and her help in this experiment were very valuable. From the beginning to the end, she is always involved, and I am quite indebted for the success of the experiment and analysis.

About all the oversea people I am obliged to, I thank you for all the work done at JLab. It was nice to work in this Hall C atmosphere, not forgetting night shift discussions, dinners at Plaza Azteca or Uno and soccer games. I would also like to thank especially Digpangkar Dutta, John Arrington, Paul Gueye and Rolf Ent. They always took time to answer all the urgent questions I had, and their support was very valuable to me.

For their participation to this project, but also for the whole life during my PhD years, I want to acknowledge people from the Basel group. It is a changing ensemble, but I am grateful to you for the whole time we shared in the different places over the world, Marko, Darko, Thomas, Benedicte, Roman, Beat, Giusi, Markus, Hartmut, Mark, Igal, Silvia, Gunther, Beni, Glen, Adrian, Felix. And Youri.

I want also to mention Peter Schmid, Hartmut and Roman for maintaining alive the computers, even if it looks not so easy some time.

Of course, I have to make a special mention to the French team, Thierry, and my two successive office mates, my brothers in Physics, Cédric and Fréderic for the incredible oversea and over Rhein adventures.

To finish, thanks to my family that supports me during this time, and especially to my son Guilhem.

Abstract

Experiment E97-006 was performed at Thomas Jefferson National Accelerator Facility in Virginia to measure the strength of the spectral function $S(E,k)$ via (e,e'p) for C, Al, Fe and Au at large E and k. The spectral function $S(E,k)$ describes the probability to find a proton with removal energy E and initial momentum k in the nucleus. The goal of the experiment is to study nucleon-nucleon short range correlations that occur in nuclei due to the short range and tensor nucleon-nucleon interaction.

Data were taken in parallel and perpendicular kinematics for the different targets. Electron and proton are detected in coincidence in two spectrometers which allows reconstruction of missing energy (E_m) and missing momentum (p_m). In the Plane Wave Impulse Approximation E_m and p_m are related to the absolute value of the initial energy E and the initial momentum k of the nucleon inside the nucleus. The deradiated spectral function for each nucleus can be extracted from the experimental data via an iterative process.

However, the region of high E_m and high p_m is contaminated by multi-step processes, rescattering of the knocked-out nucleon and Δ-excitation. The kinematics was chosen to minimize those effects but they are still significant and need to be corrected for. For that purpose, different kinematics and a variety of nuclei were used in the experiment to allow by their comparison to shed some light on those effects. Theoretical corrections as an additional handle on the multi-step processes are being computed.

The comparison with calculations reveals various discrepancies with the data. On one hand, for the parallel kinematics, which minimises the influence of FSI, one finds roughly agreement. On the other hand, the perpendicular kinematics confirm the importance of the FSI, the spectral function being bigger than the parallel experimental one. The use of the different targets emphasises this behavior; the FSI contributions, which increase with the target mass, tend to overwhelm the correlated region.

Contents

List of Figures

List of Tables

1 Introduction

Electron scattering experiments are at the source of some important knowledge about nucleus and nucleon structure. This well understood probe, originating from a good description of the electromagnetic interaction by Quantum Electrodynamics, allows to quantitatively investigate nuclear systems. With a simple approximation of the exchange of one virtual photon carrying the transferred momentum and energy to the nucleus, it is possible to access a wide range of information.

The nucleus may be seen as an ensemble of nucleons where each nucleon interacts with the other ones. When using a mean field approximation, it gives rise to the shell structure that was already experimentally confirmed many years ago [1]. Other components of the nucleon-nucleon interaction are not taken into account in this approximation such as the short range interaction.

Short range correlations are a general phenomenon in physics [2], and are encountered in various fields. Atoms or ^3He droplets may be seen as fermion systems that experience such an interaction. Its relative strength gives rise to effects that are more or less pronounced. For example the depletion of shell in ^3He droplets is close to 50%.

It is commonly accepted that correlated nucleons account for approximately 15-20 % of the ground-state nuclear wave function. Yet, despite of many years of experiments, little is known about the nature of these correlations. The reason: it is very difficult to distinguish experimentally between short-range correlations and competing two-body processes and currents such as final state interactions or meson-exchange currents.

The Thomas Jefferson National Accelerator Facility (TJNAF) offers the possibility to measure the cross section of electron-nucleus scattering for different kinematics and different target nuclei. Several experiments were already performed in the quasielastic domain to extract the spectral function, but they only give access to the single-particle structure of the target, and thus the mean field approximation may be tested. The experimental spectral function in the correlated region was measured in the experiment E97-006 at TJNAF. The necessity to investigate the spectral function at high momentum and energy was the lack of information in this region and the need to study the reaction mechanism. This experiment is the subject of this thesis.

The analysis of the data for four different targets and two kind of kinematics provide good tests for the short range interaction and Final State Interactions (FSI) or Multi Step Processes(MSP).

2 A(e,e'p) reaction and Plane Wave Impulse Approximation

In our experimental process, we have to deal with two different kinds of interactions. The first one is the scattering of an electron on a proton. It is a well established procedure to first consider a free proton and to then add corrections to this description. The simplest case that we will work with, is called the Plane Wave Impulse Approximation and is briefly described in the following section.
The second part is linked to the fact that the proton is in the nuclear medium and so it is feeling the interaction with the surrounding nuclear matter. For this part several models were developed such as optical or Glauber model.

2.1 Plane Wave Impulse Approximation

The Plane Wave Impulse Approximation (PWIA) consists in looking at the reaction assuming that the incoming and outgoing particles may be seen as plane waves. It requires three basic assumptions. First the scattered electron transfers momentum and energy via only one virtual photon. Then this virtual photon couples to only one constituent of the nucleus. And finally, the final state interaction of the knocked-out nucleon with the (A-1) residual nucleus can be neglected.

The Feynman diagram for this description is shown in figure 1. The left side represents the incoming and outgoing electron with respective energies, E_e and $E_{e'}$. A virtual photon transfers the momentum $\overrightarrow{q}$ and the energy ν to the nucleus. The four momentum transfer is defined as $Q^2 = q^2 - \nu^2$. The virtual photon couples to a bound (off-shell) nucleon that carries a momentum $\overrightarrow{k}$ and energy E_p. After the scattering process, the knocked out nucleon carries a momentum $\overrightarrow{p} = \overrightarrow{k} + \overrightarrow{q}$, while the residual (A-1) system is left, generally in an excited state, with a momentum $-\overrightarrow{k}$.

Two quantities may be defined in the study of such a reaction, the missing energy, E_m and the missing momentum, p_m.

$$E_m = E_e - E_{e'} - T'_p - T_{rec} \tag{1}$$

$$\overrightarrow{p_m} = \overrightarrow{q} - \overrightarrow{p} \tag{2}$$

When considering the PWIA, we can identify the missing energy E_m with the initial energy of the nucleon E_p, and the missing momentum, p_m with the opposite of the initial momentum of the struck nucleon $\overrightarrow{k}$. The remaining nucleus is thus considered as not

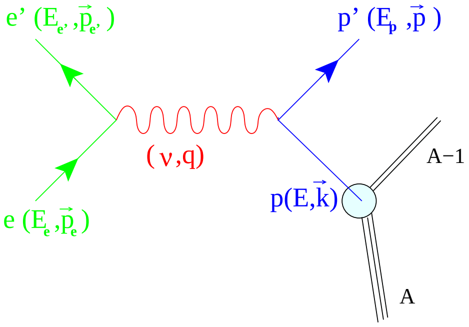

Figure 1: One Photon Exchange for a nucleus.

participating in the reaction. Its recoil energy is taken into account.

2.2 Nucleon-Nucleon Interaction

The knowledge we acquired in the past decades about the interior structure of the nucleons lead us to consider the whole hadron from the quark point of view. In this approach Quantum ChromoDynamics should be able to describe the nucleons and the interaction among them. The interaction between nucleons may be considered as the resulting residual strong interaction that occurred between quarks. In fact, the complexity of the many body problem makes a calculation not yet possible, and we have to consider phenomenological nucleon-nucleon interactions.

The short range interaction results from the repulsive part of the nucleon-nucleon interaction. The attractive part gives rise to the binding of nuclei and is used to describe the single particle properties of the nuclei. Well studied and well known, this part of the interaction has been verified to explain the properties of many nuclei.

For nuclei, we face a many-body problem for which exact solutions are not feasible at this time. For Carbon, solutions of the Schrödinger equation for realistic N-N interactions are becoming possible. But for heavier nuclei approximations are needed in order to compute their wave function.

2.3 Independent Particle Shell Model (IPSM)

As mentioned before, it is the model used to describe the shell structure of the nuclei. All the participants are seen as independent of each other moving in the mean field created by the surrounding nucleons. This model is well established now, and a number of approaches using different potential models have proven to describe correctly several experimental properties of the nuclei. These potentials are obtained either by Hartree-Fock calculations using an empirical effective nucleon-nucleon interaction, or taken as a phenomenological optical potential, mainly of Wood Saxon shape, with parameters obtained from fits of elastic proton scattering on the considered nucleus. The success of this picture to explain many experimental data, e.g. results from Almadi *et al.* [1] for carbon and aluminium with experiment (p,2p) in the sixties (figure 2), was already giving credit to this description. Nowadays with extensive experiments on various nuclei, it shows its pertinence.

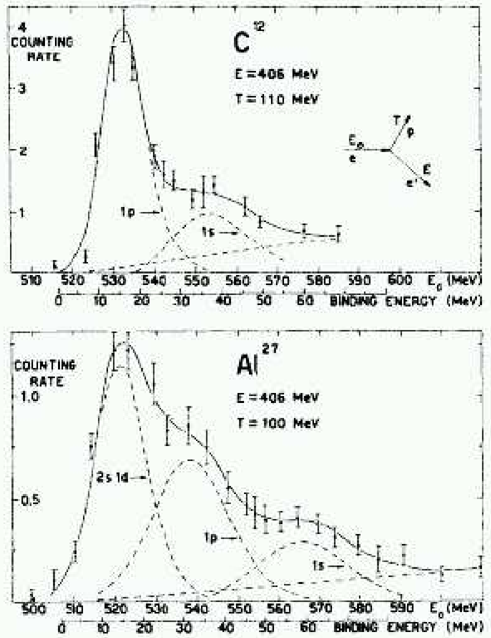

FIG. 2. Electron-proton coincidence counting rate per 10^{11} equivalent quanta at 550 MeV as a function of the incident energy. The dashed lines indicate the contributions of the various shells and the background as explained in the text.

Figure 2: Experimental energy shells for ^{12}C and ^{27}Al from [1].

However, some quantities such as the occupation probabilities are far from the expected theoretical value. In an IPSM scheme, they are supposed to be equal to one which corresponds to full occupation of the orbital. Any deviation from this value has to be seen as the signature of physical processes that are not fitting in this picture. In figure 3, we clearly see that for lead the occupation probability is lower than 1, the values between 0.5 and 0.75, indicate that the theory is not explaining at least 25% of the nucleons. The mean field only deals with nucleons in states occupying single-particle states below the Fermi energy, it fails to describe any nucleon which is not in them. Figure 4 emphasises the fact that the depletion of the states below the Fermi energy is not restricted to one sole nucleus, but is a more general phenomenon. The relatively constancy of the value of this depletion over a large mass region is leading to the explanation of a process independent of the mass number, such as correlation effects. There are two kinds of such interactions. The first one are the so-called long-range correlations and are related to collective modes of the nucleus. They are believed to cause 15-20% of the depletion. With the 65 % remaining in the mean field part, the short range and tensor correlations account for the last 15-20%. These values may vary from different theoretical descriptions, but the range is roughly determined.

Short range correlations are linked with the strong repulsive interaction occurring between two nucleons at very short distance. The two nucleons are then scattered with high opposite momentum k and high energy $\frac{k^2}{2M_N}$, to states way above the Fermi surface. The consequence is the depletion of the IPSM region at low energy and momentum. According to this simple picture, a maximum at $\frac{k^2}{2M_N}$ of S(E,k) is providing a signature for the correlations.

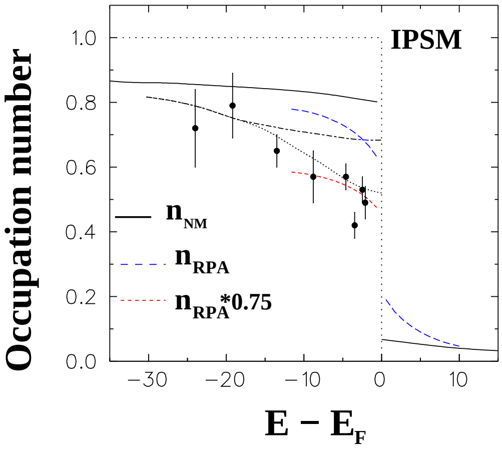

Figure 3: Occupation probability for lead. The experimental data differ from 1, thus providing a signature for correlations.

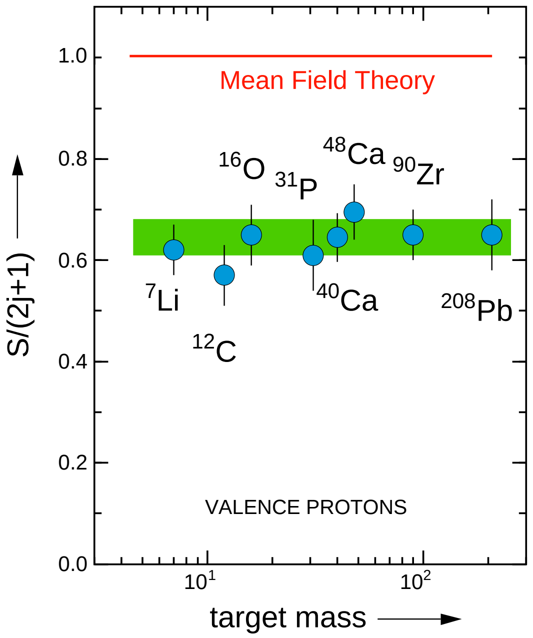

Figure 4: Spectroscopic factors for various nuclei.

2.4 The spectral function

The spectral function S(E,k) is the probability to find a proton with E and k in the nucleus. In a PWIA approach, one may factorize the differential scattering cross section with :

$$\frac{d\sigma}{dE_{e'}dE_p d\Omega_{e'} d\Omega_p} = K\sigma_{ep}S(E,k) \tag{3}$$

This factorization offers us a tool to investigate the structure of the studied nucleus. The first part, σ_{ep}, is related to the scattering process and the nucleon is pictured as a composite object described by its charge and magnetic form factors where σ_{ep} may be calculated following the prescription of De Forest [15]. The second part accounts for the structure of the nucleus.

As we see later, this framework is still used in the case of the distorted wave impulse approximation where the factorisation of the differential cross section gives access to a quantity called Distorted spectral function or reduced cross section. If, by suitable choice of the kinematics, the distorsion effects can be minimised, one still can get access to the spectral function.

2.5 Infinite Nuclear Matter and Correlations

Several theories deal with the study of the nuclear spectral function. If exact calculations are possible for light nuclei via for example, variational Monte Carlo, or infinite nuclear matter, for the rest of nuclei, approximations and extensions based on the mean field framework are often used. These calculations are not adequate to describe the high momentum and energy region. Techniques like Green's functions theory are used now [13]. The correlated basis function (CBF) approach from Benhar [3], [4], gives good agreement with existing data for (e,e'), and is used in this work for the comparison with the experimental data.

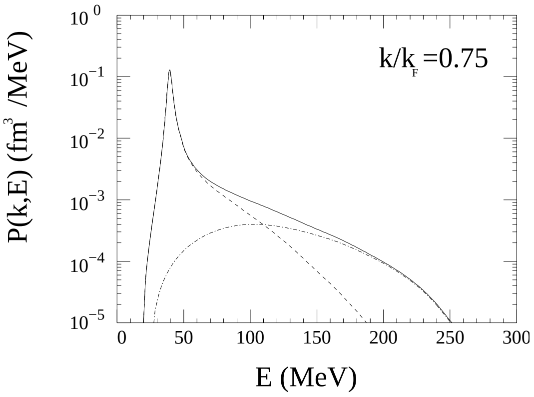

Nuclear matter spectral function

Figure 5: Infinite Nuclear Matter Spectral Function. The solid line gives the full spectral function, the dashed, and dot-dashed curves give the single particle part and correlated part, respectively.

For comparison to our data, the theory has to describe correctly the spectral function in both the single particle aspects and the short range correlation properties. The former concerns the region of low momenta and removal energy, whereas the latter deals with the high momentum components and high energy. To achieve this description the calculation of the spectral function is made with a combination of the nuclear matter and finite nucleus mean field spectral function. The separation of the spectral function in a single particle part $S_{sp}(E,k)$ and a correlated part $S_{corr}(E,k)$ allows to treat separately these two physics features.

To obtain the correlated spectral function for finite nuclei the dependence of the spectral function on matter density is calculated. From the calculation for infinite nuclear matter it is then possible to obtain the spectral function for finite nuclei via the local density approximation (LDA).

The correlated part arising from the LDA calculations accounts to 22% for carbon, to 20.7% for gold relative to the total strength. We used for the quasi-hole part the IPSM spectral function normalised in such a way that the integrated sum of the two parts is giving the number of protons in the nucleus.

In the region below the Fermi momentum and for small energies S(E,k) is dominated by the quasi-hole peak and the correlated contribution appears only as background. Proceeding to large E the correlated part dominates even at small momenta like it is pictured in figure 5. It is also worth to emphasize that the correlated spectral function also contributes to single particle region. This means that in most cases the spectroscopic factors measured in experiments not only contain the quasihole contribution, but also a background contribution from the correlated part. This is true in particular when the spectroscopic factor is integrated over a selected energy region.

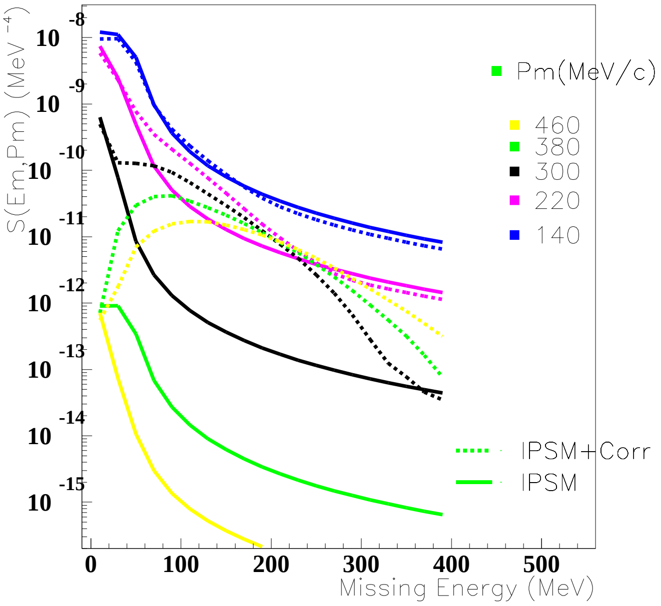

Figure 6: Spectral function resulting from the sum of the IPSM part and the correlated part from Benhar (dashed) and the IPSM spectral function alone (solid line).

From the result of the CBF calculation for infinite nuclear matter (figure 5), we may see already various features that will be also present in the experimental data. We can see it as a superposition of two different parts, the first one is related to the nucleons in the single particle region, leading to the shell structure, the other one is linked to the correlations and gives rise to components of high momentum and high energy.

2.6 Momentum and energy distributions

In general the momentum distribution $n(k)$ can be obtained by integrating the spectral function over the whole range of missing energy.

$$n(p_m) = \int_0^\infty dE_m \cdot S(E_m, p_m) \tag{4}$$

When using experimental data one is restricted to the range covered by the experiment. Further we are only interested in the correlated part. Therefore to exclude single particle states the lower limit is set to 60 MeV. The upper limit is determined and restricted by the occurrence of other reactions. It thus depends on the momentum because small k implies small E. By integrating the weighted momentum distribution with the squared momentum over k gives access to the number of proton Z_p detected in the chosen fraction of the correlated region. The spectroscopic sum rule ensures that the integration over the whole range in energy and momentum is giving the total number of proton contained in the nucleus.

$$Z = 4\pi \int_0^\infty dp_m \cdot {p_m}^2 \cdot n(p_m) \tag{5}$$

3 Final States Interactions

In the process we are looking at, there are other reactions that can mimic strength in the regions of interest. Two kinds of secondary reactions, neglected in the PWIA, can play a role, multistep processes and Δ excitation.

3.1 Delta Resonance

The first one is the excitation of the knocked out proton in a Δ; the deexcitation via the emission of a pion may simulate a large missing energy and missing momentum. The large missing energy comes from the undetected mass of the emitted pion, and is expected to have an influence on the spectral function at large values of energy. The transverse character of this reaction provides a kinematical help to reduce this contamination, as it

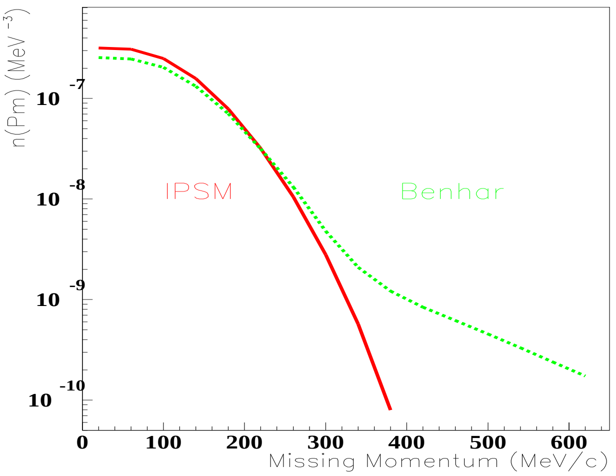

Figure 7: Carbon momentum distribution, the red solid curve corresponds to the IPSM model and the green dashed curve corresponds to the model including the correlations from the Benhar calculation.

appears preferably at large angle between the initial momentum k and the momentum transfer q.

One important fact is that the corresponding protons have lost at least an energy of 140 MeV corresponding to the mass of the pion.

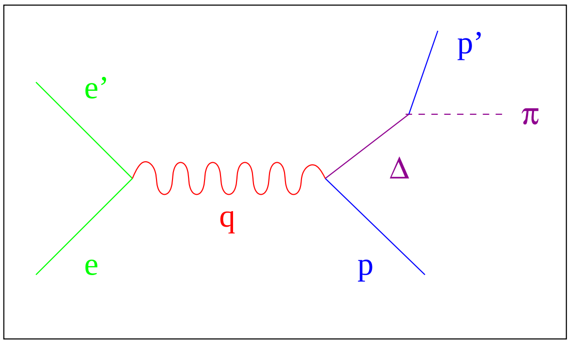

Figure 8: Δ excitation.

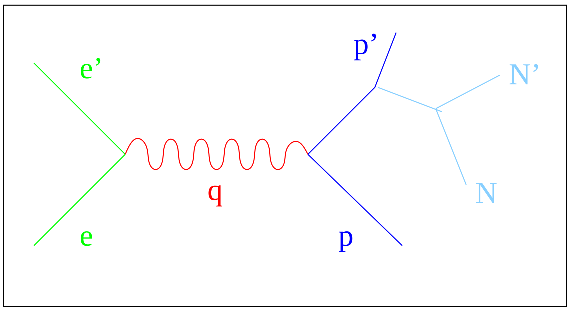

Figure 9: rescattering process.

3.2 Nucleon Rescattering

The second process is the rescattering of the knocked out proton by a nucleon of the residual nucleus. The proton gets therefore a different energy and momentum and this misleads the reconstruction of E_m and p_m. Because this process happens with the nucleons from the residual nucleus, its strength depends on the size of the nucleus. On the other hand, the correlations occur at short range, and only the next neighbours are involved. As a consequence, the correlated strength is expected to be independent of the size of the nucleus. The use of several targets regularly spaced in $A^{1/3}$ is thus offering a tool to probe this contribution. Simulations from [12] in parallel kinematics show that the process moves mostly strength to larger E and smaller k. This contribution is minimized in parallel kinematics above the ridge.
A recent article by Barbieri [24] shows that it is possible to explain part of the excess strength of the spectral function in these regions by this process.

4 Radiative Corrections

Another important physics phenomenon for the analysis is the radiative effect from internal and external Bremsstrahlung. The Feynman diagrams illustrating this process are shown in figure 10 and 11 for the electron and the proton.
Internal Bremsstrahlung means that the electron radiates real or virtual photons in the processes of scattering from the nucleus. It is independent of the target thickness.
External Bremsstrahlung means that the electron radiates in the Coulomb field of any nucleus other than the one involved in the scattering process. It therefore depends for example on target thickness.
This implies that incoming and outgoing particles have some radiative emissions that

modify the kinematics of both particles.

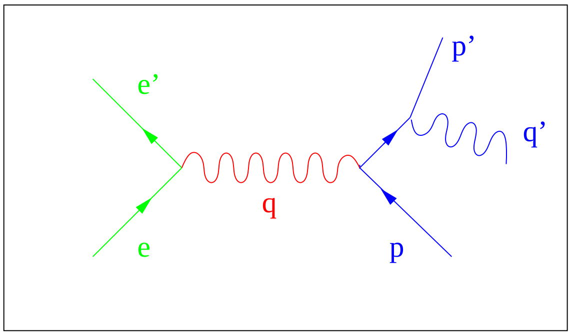

Figure 10: Bremsstrahlung for knocked out proton.

To correct for these effects, a code developed and used in experiments at the Stanford Linear Accelerator (SLAC) is used [10]. The code uses the formulae of Stein *et al* [18], followed by the work of Mo and Tsai [19],[20]. New calculations made in Basel by Weissbach, improving upon the peaking approximation, are underway.
For this analysis, the recipe from Dutta adapted to the TJNAF software analysis[6], [7] was used.

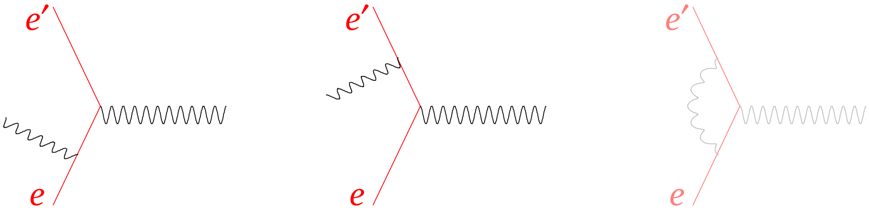

Figure 11: Bremsstrahlung for the electrons. The third diagram shows an example of second order corrections.

5 Kinematics

As shown in the figure 12, two kinds of kinematics are of interest in experimental studies. The first one, called perpendicular kinematics, corresponds to an angle between the virtual photon momentum and the initial proton momentum of $\approx$ 90 degrees. For the parallel kinematics this two quantities are taken parallel.
Our experiment was planned with two different perpendicular kinematics and three parallel ones.

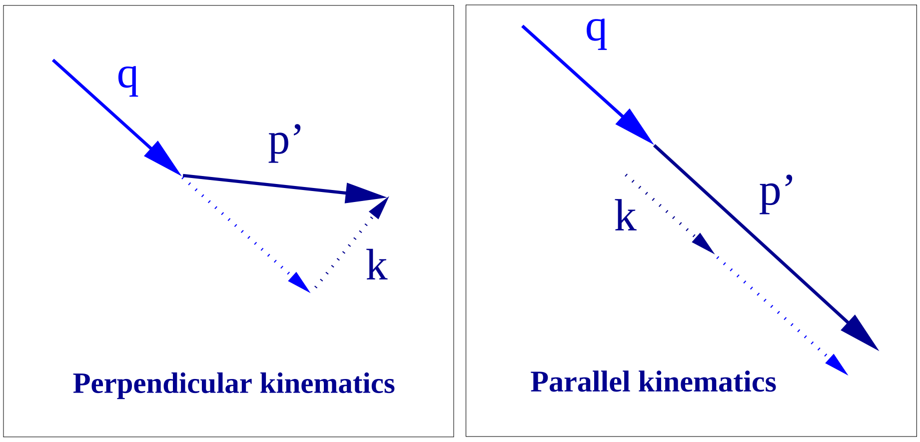

Figure 12: Kinematical conventions; the "parallel" and the "perpendicular" labels are related to the angle between the virtual photon momentum and the initial proton momentum.

The covered regions in the (E_m,p_m) plane are shown in figure 13. They allow to work in regions from 200 to 700 MeV/c for p_m and 0 to 400 MeV for E_m in parallel and from 100 to 800 MeV/c in perpendicular kinematics. This should allow a study of MSP, considering the fact that the MSP are favored in perpendicular kinematics. Even if in parallel kinematics, these processes are not entirely suppressed, one may hope to correct for them using theoretical calculations calibrated in perpendicular kinematics.
The chosen kinematics were determined following the calculations made by Rohe, Tiefenbacher and Zao.

6 The Quest for Short Range Correlations

Many other experiments have been done or scheduled in order to isolate SRC in nuclei. Either A(e,e'p) and A(e,e'pp)X have been employed to investigate them. It is often

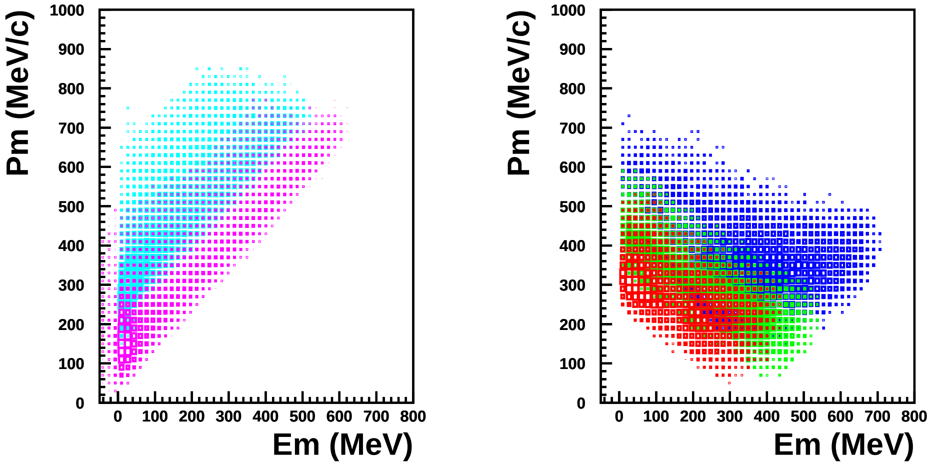

Figure 13: Kinematical regions covered by the experiment; up to 800 MeV/c for p_m. The events at negative E_m are accidentals.

argued that the use of Rosenbluth separation which gives access to the transverse and longitudinal part of the cross section, is helpful to deal with the problem of Δ excitation and MSP. If for the inclusive reaction (e,e') this separation is of interest, it is no more true in the case of exclusive process. A study of the existing data [12], does not show any fact supporting it. The transverse nature of the Δ cannot be helpful in this way, but may give some information in the analysis of the data.

Most of the previous experiments found a large excess in the strength as compared to what was predicted in PWIA. This most likely is due to the choice of the kinematics, which allowed for reaction mechanisms other than PWIA as described before. Further from purely kinematical arguments it is clear that for parallel kinematics the large final momentum of the knocked out proton is directly connected to a large initial momentum via scattering, whereas in the standard perpendicular or anti-parallel kinematics the same final momentum can occur due to smaller initial momenta plus multiple scattering. These contributions then overwhelm the cross section due to much larger spectral function at values of k' and E' where the strength originates from.

In this experiment, the contributions of the delta and rescattering to the correlated region are minimised in parallel kinematics.

Part I

Experiment

TJNAF is an electron accelerator equipped with three experimental halls in which one can run experiments with different energy and current intensity. For the e97-006 experiment, a continuous wave (CW) unpolarised electron beam of 3.2 GeV and maximal intensity 60 μA was delivered to Hall C. The electrons scattered on hydrogen, carbon, aluminium, iron and gold targets. The scattered electrons were detected with the High Momentum Spectrometer (HMS) and the knocked-out proton by the Short Orbit Spectrometer (SOS). The kinematics used in the experiment are summarized in the following table.

Kinematics	beam energy	θ HMS	momentum HMS	θ SOS	momentum SOS
	Mev	degrees	Mev/c	degrees	Mev/c
p1	3296.9	12.5	2750	73.0	1000
p2	3296.9	12.5	2750	70.0	850
3	3296.9	12.5	2050	29.0	1700
4	3296.9	12.5	2400	30.0	1500
5	3123.3/3120.0	12.5	2500	38.0	1250

Table 1: Details of kinematics

7 Accelerator

The thermionic gun of the injector delivers electrons with an energy of 10 keV. Two chopping cavities are used to give each hall the required beam intensity. For this the beam is swept on three chopping apertures which determine both the current for the individual halls and chop the beam into beam bursts of 1.67 ps. Then the beams are recombined and accelerated to 45 MeV.

The main accelerator is composed of two superconducting linear accelerators (linacs) and two recirculating arcs allowing the electron to pass several times through each linac. Each linac has 20 cryo modules and accelerates the electrons by 400 MeV (nominal tune).

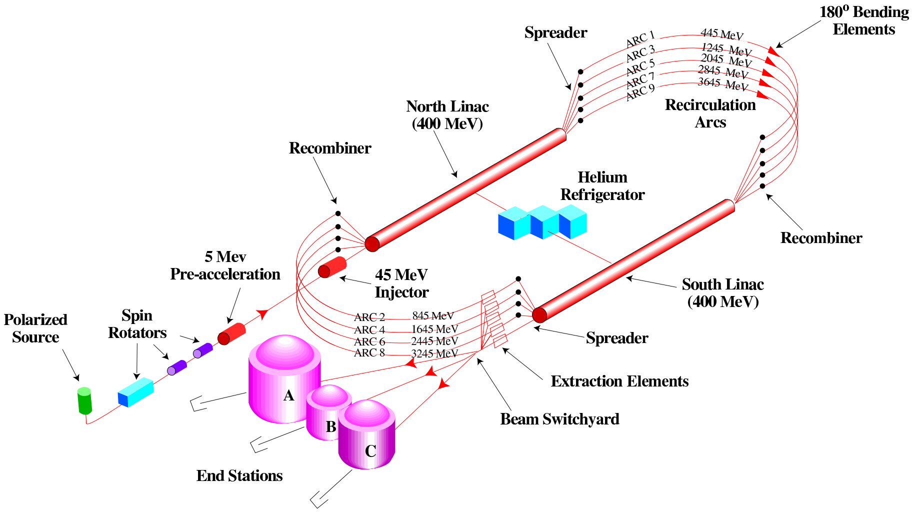

Figure 14: TJNAF accelerator. The three halls are supplied with beam after several paths in the linacs.

8 Hall C Beam Line

After being accelerated to the requested energy, the electrons are extracted in the beam-switchyard and travel to the 42m long Hall C arc. The arc bends the electrons by 34.4° and may be used to measure the beam energy. Moreover, in and after it, several devices are used to measure beam position, current and profile.

8.1 Beam Position Monitor

During the experiment, the Beam Position Monitors (BPM) were used to monitor the beam position, its shape and its angle relative to the nominal 0 deg line. Each BPM is composed of four antennae located at ±45° relative to horizontal and vertical planes. The intensity of the pick-up signal is proportional to the distance between the antenna and the beam. The position is determined from the ratio of the signals of two opposite antennae. In first order the use of the ratio makes this measurement independent of the current. By using several BPM, the angle at the target may also be determined.

The superharp is made with a tungsten wire that is moved through the beam by a stepper motor. The accuracy of this method is $\pm 200 \mu m$. As it disrupts the beam, it is not usable during production time.

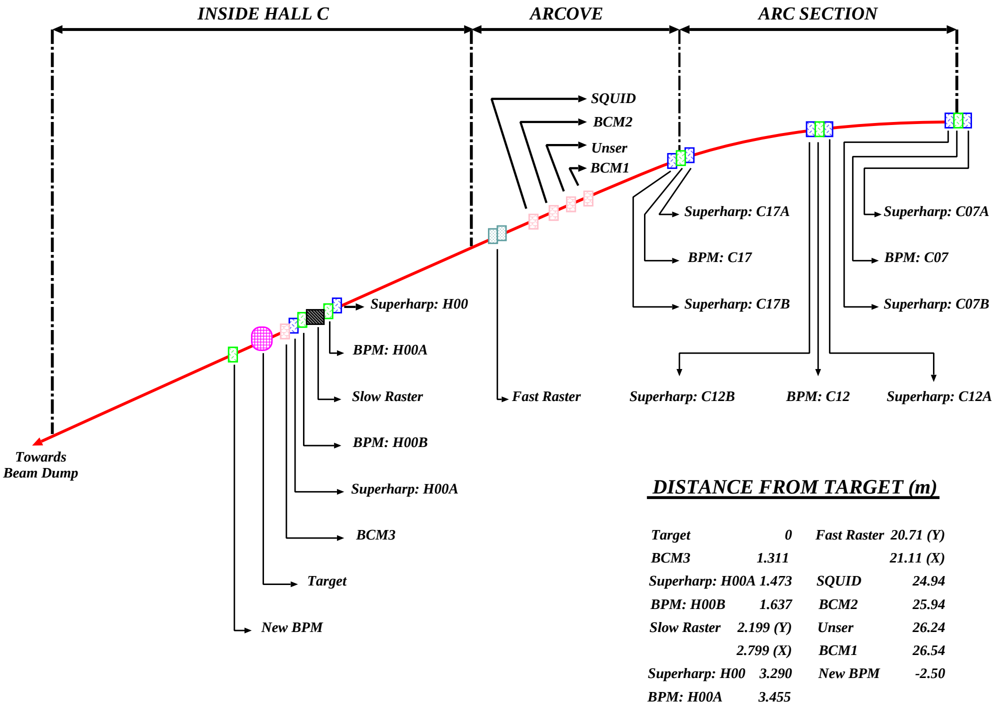

Target	0	Fast Raster	20.71 (Y)
BCM3	1.311		21.11 (X)
Superharp: H00A	1.473	SQUID	24.94
BPM: H00B	1.637	BCM2	25.94
Slow Raster	2.199 (Y)	Unser	26.24
	2.799 (X)	BCM1	26.54
Superharp: H00	3.290	New BPM	-2.50
BPM: H00A	3.455		

Figure 15: HallC beamline.

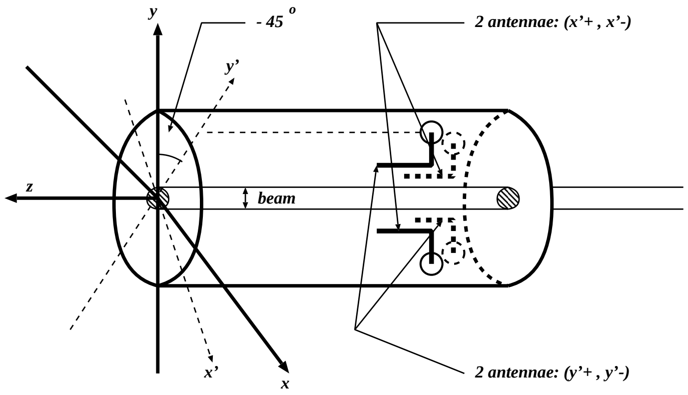

Figure 16: BPM

8.2 Beam Current Monitor

For the calculation of absolute cross sections, it is very important to get an accurate knowledge of the integrated charge, and thus of the current. The beam current in Hall C is measured with two kinds of current monitors. The Beam cavity monitor (BCM) is a cylindrical resonant cavity mounted on the beam line. The beam passing through it excites resonant modes that are picked up by wire loop antennae. The power in the antennae is proportional to the beam current squared. Some special modes of the cavity are quite insensitive to the beam position.
A dependence to the temperature of ±0.25%/°$/C$ is known. This introduces an uncertainty of ±0.3%.
The parametric current transformer (Unser monitor) is used to calibrate the gain of the cavities. The Unser monitor has an extremely stable gain but a drift in its offsets. Calibration runs were taken during the experiment to check the gains of the BCMs. All factors together yield an absolute error of 1% to 2% (for low current 10μA) for the charge measurement.

8.3 Beam Rastering

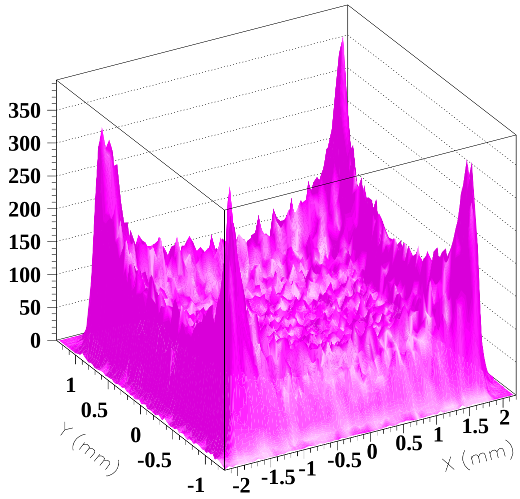

Figure 17: Beam rastering

To prevent local melting of the target by the electron beam, the beam needs to be rastered. The fast raster is located 25m in front of the target and rasters the beam with frequencies of 24.2kHz horizontally and 17kHz vertically. The result is a rectangular pattern with increased intensity at the edges of the rectangle. The rational ratio of the frequencies is chosen in order to achieve an uniform distribution of heat deposit in the targets and to avoid standing Lissajous figure.

8.4 Beam Energy Measurement

The beam energy is obtained from measurements of the total field integral $\int Bdl$ required to bend the beam through the Hall C arc. During the Arc measurement all corrector magnets are turned off. Position and direction of the beam are measured at the beginning, middle and the end of the arc. Knowledge of field integral and absolute position of the beam allows an uncertainty of $\delta E/E \leq 1 \cdot 10^{-3}$. Together with the position uncertainty, a value of $1.2 \cdot 10^{-3}$ is found for the beam energy uncertainty.

9 Targets

Both cryo and solid targets were used during the experiment. The cryo target was composed of three loops, filled with hydrogen and was used for the calibration runs. Each loop is composed of one target of 15cm and one of 4cm length. In addition, the cryo ladder provides two dummy aluminium targets used to measure the background from the windows of the cryo target cell.

The solid ladder carries carbon, aluminium, iron and gold targets. Their characteristics are described in the table 2.

Target	^{12}C	^{26}Al	^{56}Fe	^{197}Au
Thickness $[g/cm^2]$	1.25	1.08	0.49	0.48
Density $[g/cm^3]$	2.265	2.6871	7.8651	18.8146

Table 2: Target thicknesses

10 Hall C Detector Package

After the interaction with the target, the outgoing particles are detected with the two available spectrometers of Hall C. The High Momentum Spectrometer (HMS) is located on the right side of the beam pipe looking downstream. The Short Orbit Spectrometer (SOS) is on the left side. The two spectrometers have similar detection systems, but their characteristics make them more suitable for different kind of particles. The SOS spectrometer is for example ideal for the detection of short living particles due to the fact that the way between the target and the detectors is much smaller than in the HMS spectrometer.

In this experiment, HMS was used to detect scattered electrons of momenta between 2.05 and 2.75 GeV/c, at fixed angle of 12.5. SOS allowed us to detect knocked out protons of momenta between 0.85 and 1.7 GeV/c, for angles from 29.0 to 73.0 degrees.

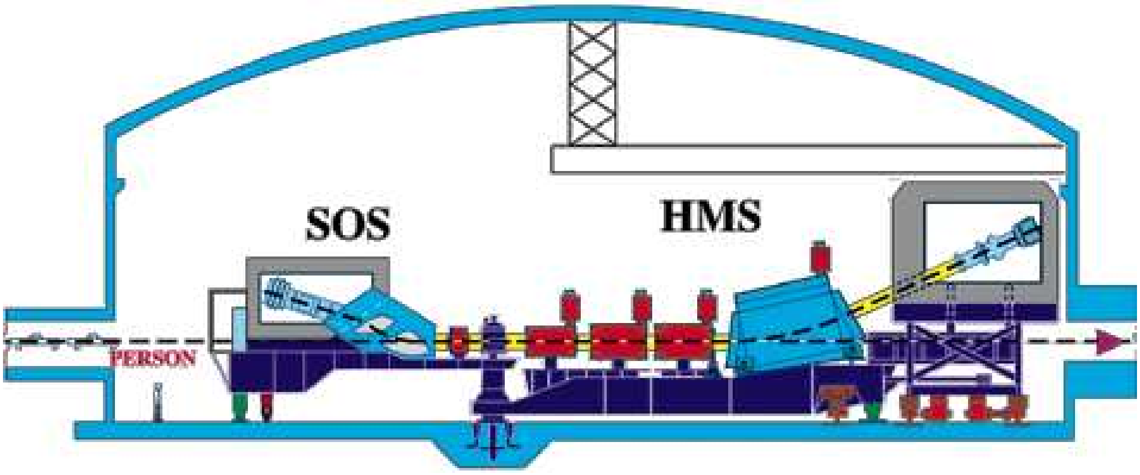

Figure 18: Hall C sketch. The beam is entering the hall from the left.

10.1 High Momentum Spectrometer

10.1.1 Description

The HMS is a three quadrupole and one dipole (QQQD) spectrometer. A quadrupole has the property of focusing in one plane and of defocusing in the plane perpendicular to it. Here, Q1 and Q3 are used to focus in the dispersive plane, while Q2 is used to focus in the non-dispersive one. This system is operated in a point-to-point tune for the central ray.

Performance	HMS	SOS
Maximum central momentum (GeV/c)	7.5	1.75
Angular range	10.5 to 85°	13.4 to 165°
Momentum acceptance	±12%	±20%
Momentum resolution	$\leq 0.1\%$	0.1%
Solid angle (msr)	6	7.5
In plane angular acceptance (mrad)	±27.5	±57.5
In plane angular resolution (mrad)	1.0	2.5
Out of plane angular acceptance (mrad)	±70.0	±37.5
Out of plane angular resolution (mrad)	2.0	0.5

Table 3: Spectrometer performances

10.1.2 HMS Detectors

The detecting system is made of two drift chambers, two pairs of hodoscopes, a gas Cerenkov detector and a lead glass shower counter. The so called focal plane (FP), is not really the focal plane of the optical system, and lies half way in between the drift chambers. For historical reasons the subscript is still of use.

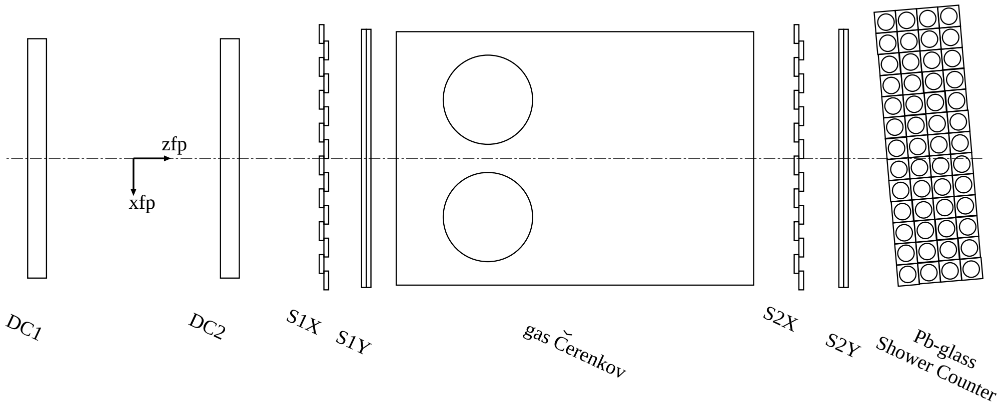

Figure 19: HMS detector package.

The drift chambers (DC) provide the tracking information. When considering both, one can extract two positions (x_{fp}, y_{fp}) and two slopes (x'_{fp}, y'_{fp}) at the focal plane. Six wire planes are used.

The hodoscopes are used as part of the trigger and to measure the particle velocity using the time of flight between the two scintillator pairs. Each pair of hodoscopes is made of two scintillator arrays with 16 scintillators in the horizontal and 10 in the vertical direction.

They cover an area of 75.5cm times 120.5cm. The bars overlap each other by 5mm. They are read out by photomultipliers sitting on each side.

The threshold gas Cerenkov detector is used to discriminate between electrons and other charge particles, mainly pions. The threshold is given by the speed of light in the medium in the tank. By choosing accurately the gas, one can get emission of light for electrons and not for pions.

The shower counters are made of four layers containing 13 lead glass bars each. The entire lead glass stack is slightly tilted in order to have no holes through which particles could pass. In lead glass, electrons deposit their full energy in a shower. They produce Bremsstrahlung photons and these photons produce e^+ e^- pairs which produce photons again. The Cerenkov light that is produced by the charged particles of this shower is collected by photomultipliers on one side of the lead glass bar. The shower counters may also be used to provide additional electron-hadron discrimination.

More detailed descriptions of all the detectors may be found for example in the thesis of D. Dutta [6].

10.2 Short Orbit Spectrometer

10.2.1 Description

The SOS is composed of one quadrupole and one dual dipole. The shorter flight path to the detection plane makes it more suitable for the detection of short lived particles. We detected mainly protons in this experiment, but some electron runs were also made. As the experiment was held close to the maximum momentum of the spectrometer, for one setting some magnet saturation effects begin to show up.

10.2.2 SOS Detectors

The same detector package as in HMS is available. Only detector sizes change, a complete description of the spectrometer may also be found in [6]. The same variables and detection techniques are applied with different ranges that are summarised in the table 3.

10.2.3 Trigger system

A complete description of the trigger system may be found in [11] or [9]. In E97-006, a single arm trigger is used in both HMS and SOS. Its purpose is to generate a pretrigger signal when a particle arrives. In this experiment, at least 3 of 4 of the scintillator layers of both hodoscopes had to fire. For the HMS, the signal is vetoed for particle identification with the Cerenkov.

The pretrigger signals are fed into a trigger supervisor circuit (TS). It consists of two modules. One logic module has as input the pretriggers from the spectrometer trigger logic units and the TS control signal(GO, ENABLE, BUSY). Its output are HMS, SOS (single) and COIN (coincidence) pretriggers and triggers, depending on the busy state of the TS. Both trigger and pretrigger signals are fed into scalers, providing information about the computer dead time. The trigger signals are then fed into a module that controls the processing of the trigger signals and initiates the readout of all ADC's and TDC's.

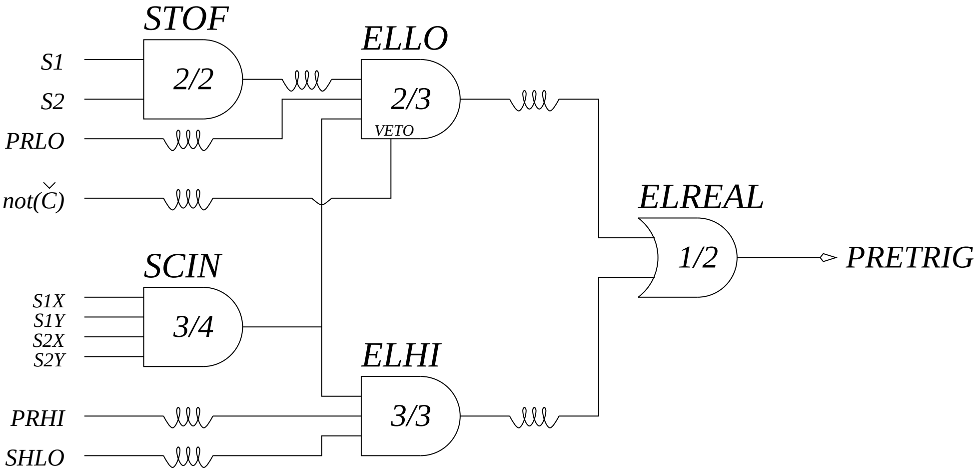

Figure 20: Single arm trigger.

11 Data extraction

Each particle must be tracked, timed, reconstructed to the target and identified, before physics quantities, i.e. E_m and p_m, can be calculated. Corrections due to inefficiencies in the detectors and processes that prevent the detection of valid trajectories must also be applied. We will describe the corrections that need to be applied to the trajectory, the standard parameters (cuts) and give a brief description of the Hall C simulation Monte Carlo (SIMC).

11.1 Optics of the spectrometers

We have two different frames in the spectrometer coordinate system that are commonly used. One has its origin in the center of the detection plane, located half way between the two wire chambers and perpendicular to the central trajectory. For historical reasons, the subscript fp (focal plane) is used. However, in the case of the Hall C spectrometers, the two planes do not coincide. Thus by definition z_{fp}=0 at the detection plane. The trajectory of a particle is characterised by its values x_{fp} and y_{fp} in the detection plane and its angles x'_{fp} and y'_{fp} with respect to the planes yz and xz.
The other frame has its origin at the target which is associated with the subscript *tar*. The trajectory of particle is characterised by the two angles x'_{tar} and y'_{tar} and the reaction point y_{tar}. In order to reconstruct the relative momentum δp to the central momentum of the spectrometer,

$$\delta p = \frac{p - p_{spec}}{p_{spec}}, \tag{6}$$

it is assumed that x_{tar}=0, so that the beam is centered at this value and that its vertical spread may be neglected. The reconstruction of the target quantities from focal plane ones is then done by means of a taylor expansion:

$$a = \sum_{i,j,k,l} A^a_{i,j,k,l} (x_{fp})^i (x'_{fp})^j (y_{fp})^k (y'_{fp})^l \tag{7}$$

With $i+j+k+l \in [0,n]$, $a \in \delta, x'_{tar}, y_{tar}, y'_{tar}$, n is the order of the expansion, and $A^a_{i,j,k,l}$ is the reconstruction matrix coefficient. These matrix elements are fitted to various data sets taken for determining the $A^a_{i,j,k,l}$'s. One check of their accuracy is made by the use of sieve slits.

11.2 Sieves slits

The sieve slit runs are taken with some special collimator grid and allow to check or redefine the matrix elements of the transport. Runs are taken for both spectrometers in order to check the validity of both systems. The figures 21 and 22 show the model and the reconstructed pattern for HMS.

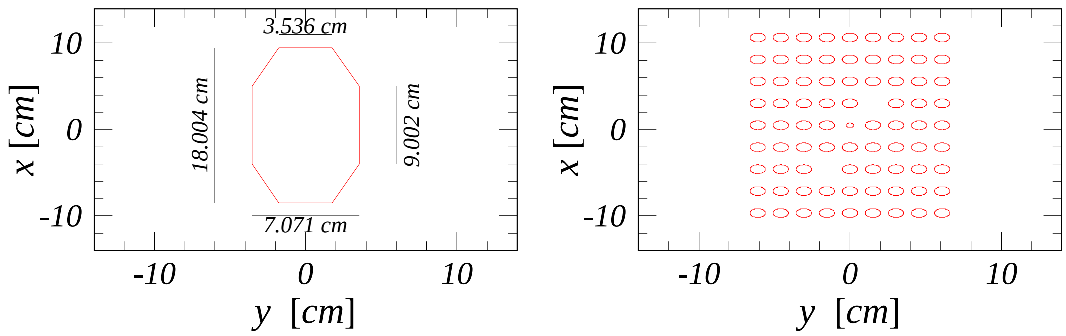

Figure 21: Sieve slits for HMS.

The two missing holes give a clear definition of the orientation of the slits. If the reconstruction did not satisfy the needs of the experiment, this data could be used together with some other dedicated runs to calculate part of the matrix elements.

11.3 Raw analysis corrections

We have several efficiencies that play a role in the acquisition, or the reconstruction of the data. The detectors have their own detection efficiencies, which need to be corrected for in order to get the real number of events involved in the reaction.
We have also to take care of the events that arrive while the data acquisition or trigger hardware is busy. To measure it, the ratio of triggers over the total number of pretriggers was taken.
These quantities were calculated on a run by run mode. The tracking efficiencies are around 97% for both spectrometers, and the dead time varies from few percent up to 30% depending on the rates in the spectrometers.

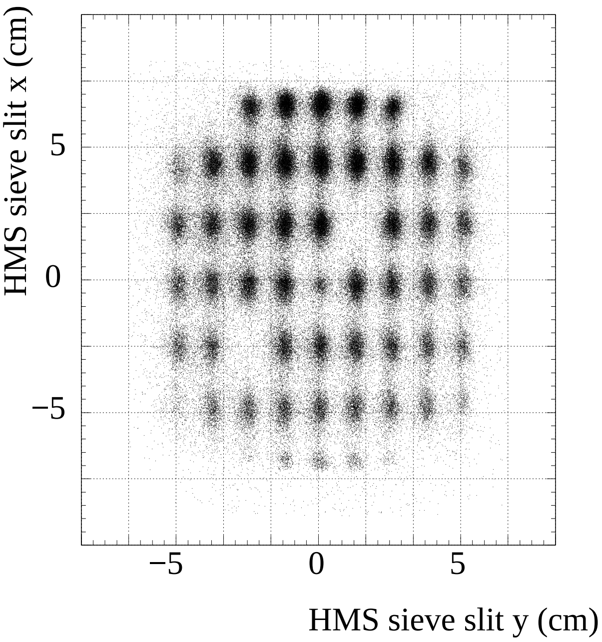

Figure 22: Sieve slits for HMS.

11.4 Background definitions

Depending on the target we have two different sources of background. In the hydrogen cryo target case, some data with aluminium targets simulating the walls were taken, and then used to correct the data.

For the solid targets, the coincidence time is used to determine the likelihood that an electron in one arm and a proton in the other arm both originated from the same reaction. It is the difference between the reconstructed times of the electron and the proton at the target, and as such is ideally a narrow peak centered at 0. The figure 23 shows a typical time spectrum for solid targets. The central peak contains the true coincidences, and the side ones are used to calculate and subtract the background that is mixed into the main peak. Background is averaged over several bunches preceding and following the coincidence time peak. We can notice that we are able to resolve the 2 ns microstructure of the beam.

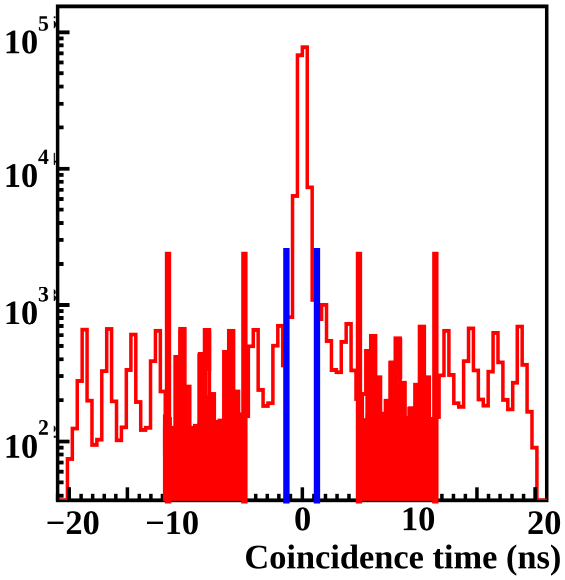

Figure 23: Background subtraction. The averaging is performed over three bumps of each side of the coincidence peak.

12 The Monte Carlo Simulation for Hall C

The Monte Carlo simulation for this experiment is done with the help of the SIMC code that allows us to generate distributions, model the two spectrometers, calculate the

De Forest off-shell cross-section, generate a PWIA spectral function and estimate the radiative correction.
It gives us valuable outputs for the analysis, in particular the phase space, depending on the experimental conditions, and the radiative corrections to apply to our extracted spectral function.
Several checks are possible using the hydrogen and the quasielastic carbon data. The good agreement between simulated yields and data allows to focus on the spectral function.
The events are generated by the Monte Carlo and after passing through various cuts are weighted by $E'p'\sigma_{ep}S(E_m, p_m)W_{rad}$; this represents the coincidence cross section in PWIA and includes a correction W_{rad} for the radiative effects.

12.1 De Forest prescriptions

The electron nucleon cross-section may be calculated using the deForest prescriptions [15]. The "off-shell" nucleon is considered on-shell, and we have a free particle-like equation:

$$\frac{d\sigma_{eN}}{dE_{e'}dE_p d\Omega_{e'} d\Omega_p} = K\sigma_{ep}S(E_m, p_m) \tag{8}$$

In the analysis and the simulation, the prescription $\sigma cc1$ was used. The prescription $\sigma cc2$ was only used as a test to estimate the accuracy of the prescription.

12.2 PWIA and IPSM spectral function

The basic spectral function used in SIMC is an IPSM one. The energy distribution of the nucleons in the nucleus is described by Lorentzian shapes, which are centered at the energy eigenvalue of a given shell. The width Γ accounts for the experimentally determined energy broadening of the shell.
The comparison with carbon quasielastic data was performed with this standard spectral function. For the extraction of the correlated strength where this IPSM spectral function is not suitable, we have to provide a new spectral function to our iterative process. The first order extracted spectral function from the data was fed into the code.

12.3 Other corrections

The radiative weight is calculated using the standard procedure from SIMC [6], [8]. Several options are available in the code, they correspond to the different models and

kinds(internal, external, i.e.) of bremsstrahlung. The option taking all these corrections into account was used.
The code offers also the possibility to correct for Coulomb corrections, raster reconstruction, multiple scattering in the huts or energy losses. For further discussion reference [8] is indicated.

12.4 Phase space

Due to the shape of the collimator, the magnets, the vacuum pipe and the detectors, the spectrometers are not uniformly illuminated over their acceptance. This means that the yield needs to be weighted by a spectrometer specific acceptance function. This is done in the Monte Carlo, and in order to extract the experimental cross section, we binned this phase space factor in E_m and p_m, the same way as the data. The same cuts are also used. After reconstruction, each bin contains an acceptance factor coefficient needed in the determination of the reduced cross section.

Part II

Hydrogen data

Hydrogen data are a very useful in order to do checks, calibrations and comparisons to models. Besides, the Hydrogen data H(e,e'p) allows us to do several checks of the experimental setup. The main reason is that there are no rescattering effects, the kinematics is overdetermined with all the outgoing particles detected and the cross section of the process is known.

The various checks that we can do are the determination of the spectrometer offsets, the estimation of the proton transmission, the checking of the experimental cross section and the radiative corrections.

For this reason, elastic hydrogen data were taken for all kinematics using the 4cm hydrogen target. The kinematics were chosen such that the central momenta of the spectrometers were the same as for the production data.

13 Offsets

Even if the spectrometer variables are known to the 0.1% level, there is still some mismatch between the reconstructed quantities E_m, p_m, W and their expected values. We have 7 parameters we can adjust offsets on: the beam energy, the two spectrometer central momenta and the two inplane and the two out of plane spectrometer angles. By varying these offsets, we can determine a set that minimises the deviations with the reconstructed quantities.

Because the reaction is kinematically overdetermined, we can make some assumptions on the following quantities:

- The invariant mass, W, should be the proton mass.
- The missing energy E_m is supposed to be equal to zero as all the participating particles are detected.
- The three components of the missing momentum P_{mpar}, P_{mperp} and P_{moop} defined as the components parallel, perpendicular to the momentum transfer vector q lying in the scattering plane and out of the scattering plane. The mean values of them should be zero.

Moreover the offsets are expected to be small, the ones concerning the momenta are fixed to a relative maximal value of ±0.4%, and the ones for the angles should not be larger than ±2mrad. Concerning the beam energy offset, two values are considered: -0.1% and -0.2%.

The offsets for the spectrometer angles are supposed to be independent of the angle and in general the offsets are taken to be constant for all the kinematics, except the one concerning the SOS central momentum; due to saturation effects in the magnets a

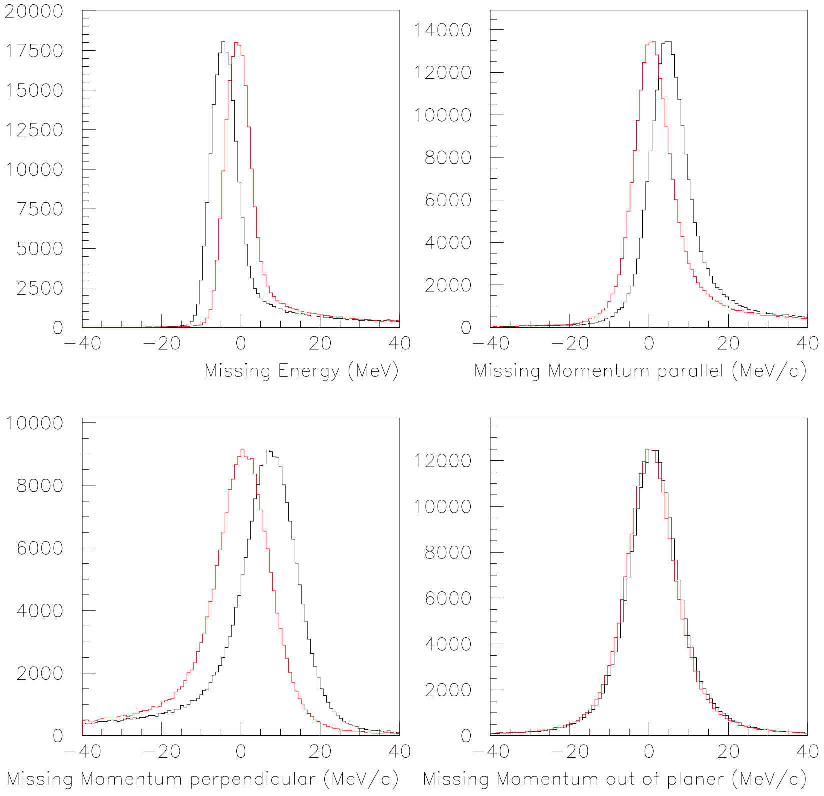

Figure 24: Mising energy and missing momentum components before(black) and after(red) applying the offsets.

dependence on the central value is expected. The results are given in the following table, and a fit to the SOS central momentum value is also provided.

E_{beam}	P_{HMS}	θ_{HMS}	ϕ_{HMS}	P_{SOS}	θ_{SOS}	ϕ_{SOS}
%	%	rad	rad	%	rad	rad
-0.1	-0.234	-0.001	0.0007	var.	0.0015	0.0007
-0.2	-0.330	-0.001	0.0017	var.	0.0015	0.0017

Table 4: Offset sets

$p_{sos} < 1.27 : 0.00225$
$p_{sos} > 1.27 : 0.00225 - 0.033 * (x - 1.27)^2$

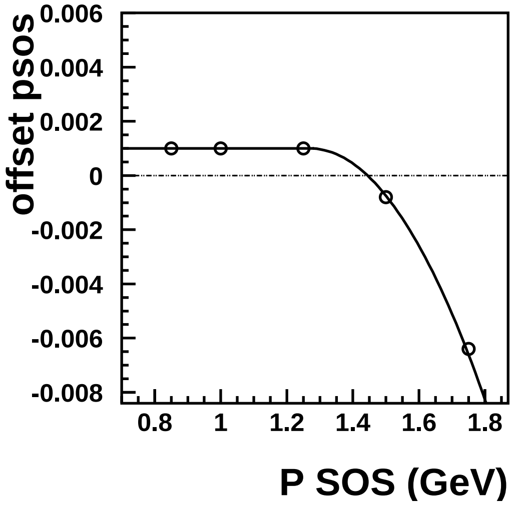

Figure 25: SOS momentum offset variations.

13.1 Proton Transmission

Because protons are strongly interacting particles, there is a significant chance they will undergo a nuclear interaction as they go through the detector stack. If such a reaction occurs and removes the proton from the acceptance before it causes a trigger, the measured yield will be artificially low. Given the nuclear interactions lengths of the materials in the proton path, it is possible to estimate this proton "absorption" [6]. It is also possible to measure it directly because every electron in the coincidence acceptance region must have caused the emission of a corresponding proton. The fraction of "missing protons" corrected for "singles" is the absorption. The proton transmission PT can be obtained via:

$$PT = \frac{N_{coin}}{N_{coin} + P_{scale} \cdot N_{e^{-}only}} \tag{9}$$

The estimate from the calculation considering all material in the spectrometer is 0.95. This results fit very well with the values obtained from the transmitted yield.

Kin.	$\perp_1$	$\perp_2$	$\|_3$	$\|_4$	$\|_5$
p mom (GeV/c)	1.0	0.850	1.7	1.5	1.25
p trans (%)	95.22	95.23	95.35	95.01	95.08

Table 5: Proton transmission

An average value of 0.95±0.005 is taken in the following analysis.

14 H(e,e'p) check

We have with this reaction the possibility to study the absolute value of the cross-section determined for the other targets.

14.1 H(e,e'p) data

The H(e,e'p) data has to be corrected for several effects in order to compare with the simulation yield. Aluminium walls are for example generating some unwanted events that can be corrected with a background estimate coming from runs taken with an empty target.

The background coming from electrons scattering off the cell entrance and exit windows was measured with aluminium targets sitting at the corresponding positions and was subtracted.

Some Δ resonance events are also seen in the spectrum; as said previously they have a higher missing energy than the events coming from the radiative tail. When separated from the rest of the yield, a look at the missing mass gives a value of around 1200 MeV (figure 27), that is close to the 1234 MeV of the Δ mass value.

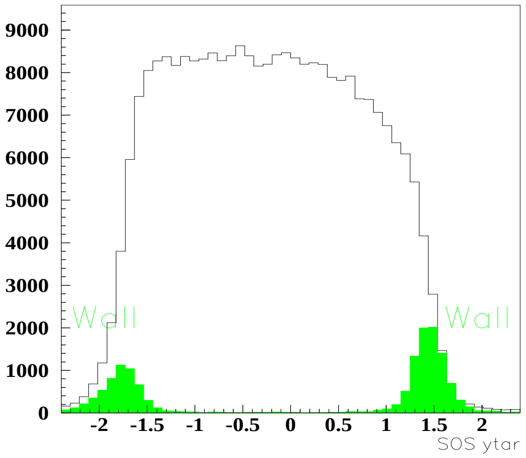

Figure 26: SOS ytar for a production run (black histogram), and for a "dummy" target run (green histogram). We easily identify the aluminium walls on the two edges of the plot.

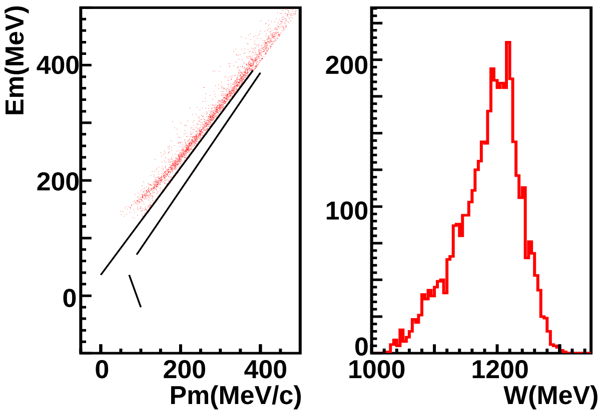

Figure 27: Delta background for ^2H data.

The corrections for all these background events may reach a value of 7% of the total yield. Clear kinematical cuts and target wall subtraction allows us to get rid off of most of these events.

14.2 H(e,e'p) data/simc ratios

The comparison of the yields from data and Monte Carlo is shown in the figures 28 and 29: it shows a fairly good agreement for target quantities.

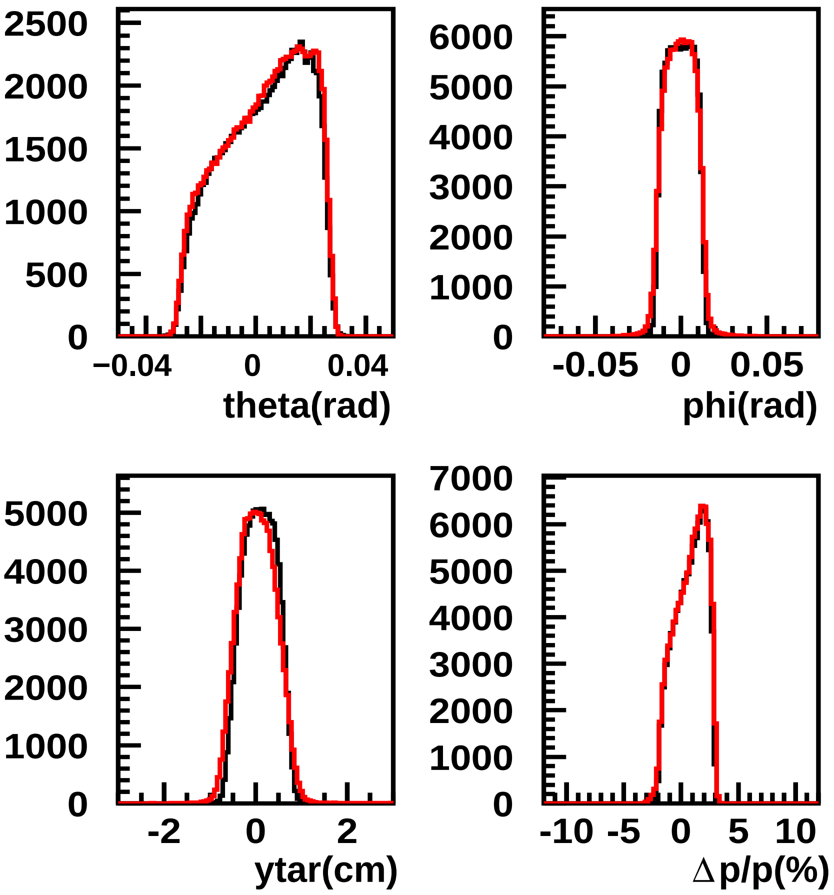

Figure 28: SIMC and data comparison for HMS variables.

The ratio of the two yields is proportional to the one of the two cross sections. We have chosen here the parametrisation given by Mergell [16].

The result is close to one with a maximum deviation of 2%.
The statistical uncertainty is negligible whereas the systematics error amounts to 2.7%.

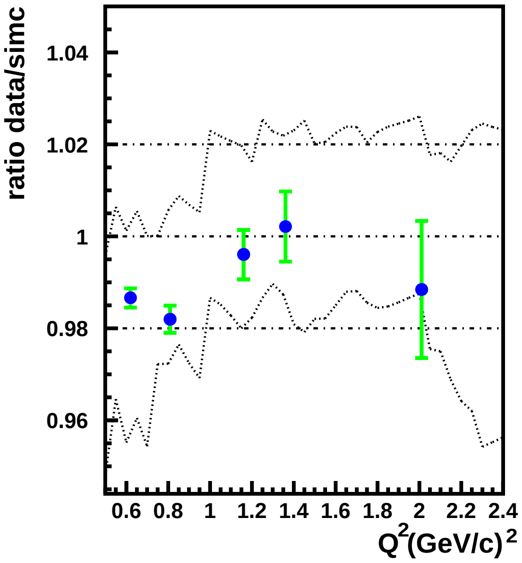

Figure 29: Yield ratio data/simulation for the 5 hydrogen kinematics. The dashed curve shows the limits according to a world data fit.

Source	evaluation %
Current measurement	1.0
Cryo target thickness	0.5
Proton absorption	0.5
Background subtraction	1.0
Constraint stability	1.0
HMS Detector efficiency	1.0
SOS Detector efficiency	1.0
Beam and spectrometer offsets	1.0
Total	2.64

Table 6: Experimental systematic errors for H_2

15 Quasielastic carbon data

Some data were taken in quasielastic kinematics for the carbon target. The central momenta were chosen as to be the same as for the production kinematics. In order to compare our results with the ones of former experiment dedicated to this kinematical region, we used in this part the same analysis method as in [6], [21] and [22].

16 Comparison with SIMC

When comparing the data with the simulation produced with the IPSM spectral function, we got a disagreement of around 20% corresponding to the effect of the tensor and short-range correlations. We can estimate for the given region the correlation correction factor from previous theoretical studies [6], [23]. For carbon a value of 1.11±0.03 is used in the present analysis.
When corrected the data show a fair agreement with the simulation (see figure 30). So the corrected IPSM spectral function is a good approximate for this region.

The single particle states of carbon $p_{3/2}$ and $s_{1/2}$ are at the expected position in energy and the shape is well described by the IPSM model(see figure 31). By integrating the yield for energies smaller than 60 MeV, we got more than 80 % of the IPSM strength, meaning that we are already including a non negligible part of the one originating from correlations.

Item	limit values
hsdelta (%)	± 11.
ssdelta (%)	± 17.
hsytar (cm)	± 3
ssytar (cm)	± 3
hsxptar (mrad)	± 0.44
hsyptar (mrad)	± 0.77
ssxptar (mrad)	± 0.55
ssyptar (mrad)	± 0.44

Table 7: Cuts used for the transparency analysis.

16.1 Transparency

The transparency is defined in a quasielastic reaction as the fraction of protons that escape from the nucleus without experiencing absorption due to FSI. With this data we can check

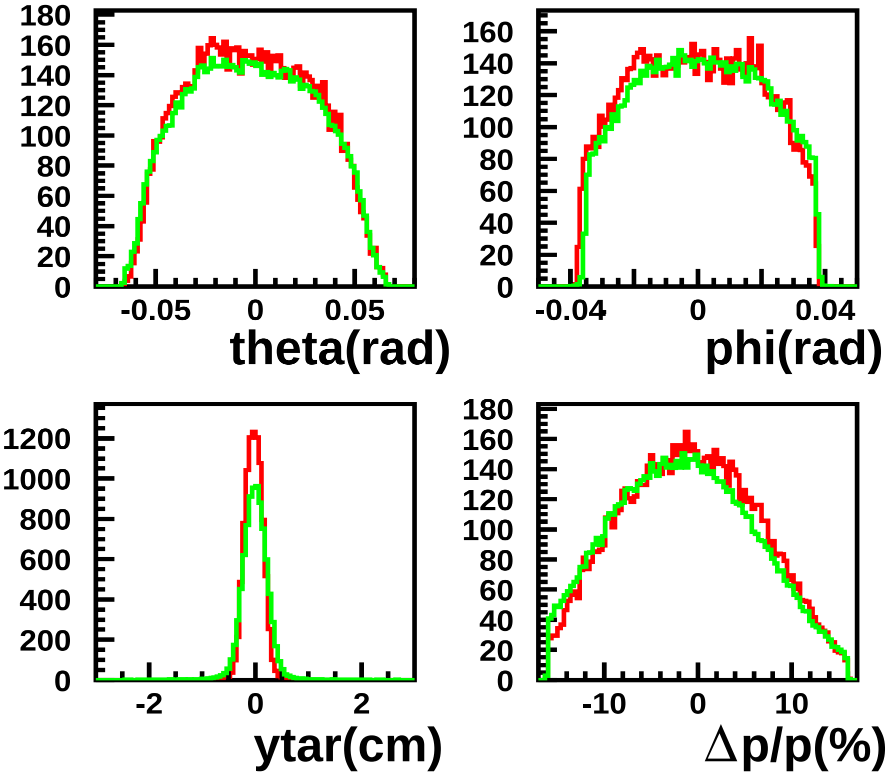

Figure 30: HMS angles and momentum for ^{12}C. Data are in green and the simulated yield is in red. Background corrections and efficiencies are included for the data yield.

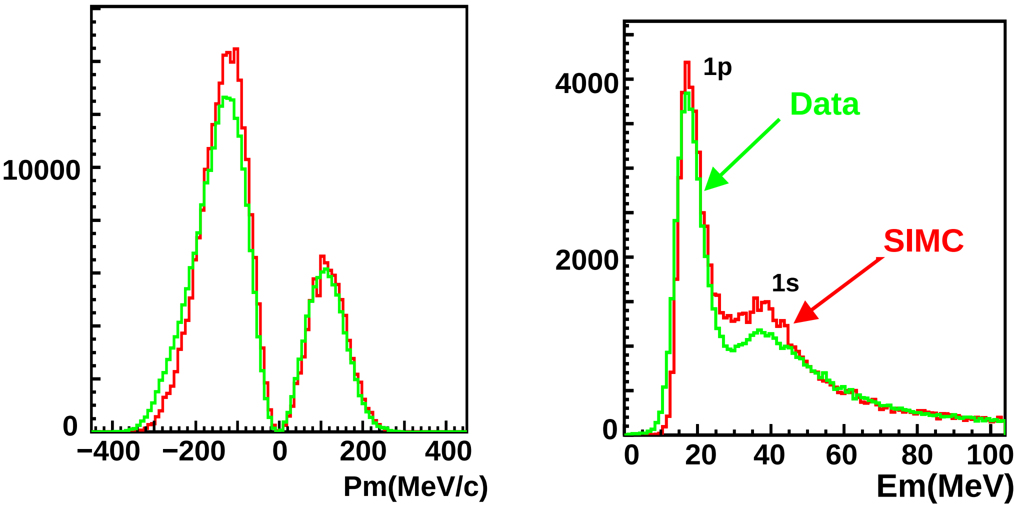

Figure 31: Quasielastic data for ^{12}C (in green). Comparison with the yield from the Monte Carlo (in red).

the consistency of the transparency for ^{12}C with the results from previous experiments carried out at TJNAF. We used the IPSM model with radiation from SIMC, as it is calculated from IA it contains no FSI. For our experimental proton yield, we take the data corrected with the correlation factor.

$$T = \frac{\int_V d^3p_m dE_m N_{exp}(E_m, p_m)}{\frac{1}{correl} \cdot \int_V d^3p_m dE_m N_{PWIA}(E_m, p_m)} \tag{10}$$

We worked with a phase volume $0 < E_m < 80 MeV$ and $|p_m| < 300 MeV/c$ as former studies have used. The results are shown in the following figure 32. We find good agreement with the points coming from experiments from Dutta [6], [21] and Garrow [22]. The consistency of this result leads to the choice for the transparency values for the analysis of the correlated region given in table 8. The figure 33 shows the experimental results for the other targets.

Target	C	Al	Fe	Au
Transparency	0.6	0.5	0.4	0.3

Table 8: Transparency values for the different targets.

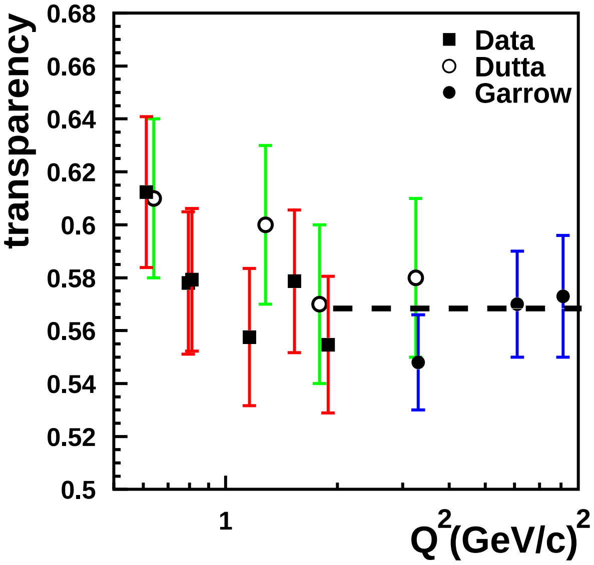

Figure 32: Transparency for ${}^{12}C$.

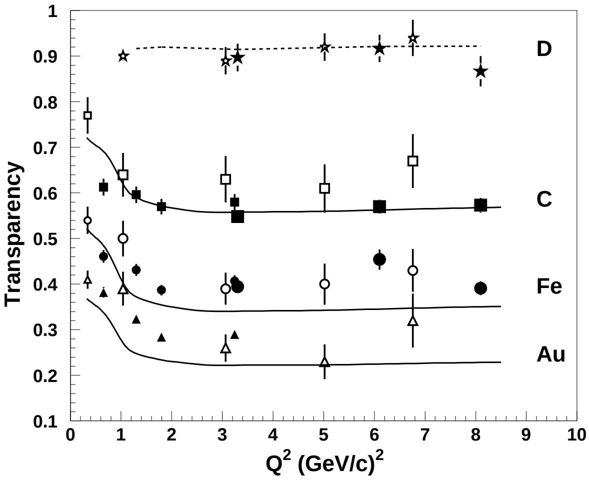

Figure 33: Transparency for D, ${}^{12}C$, ${}^{56}Fe$ and ${}^{197}Au$. The picture is taken from [22].

Part III

Data analysis

17 Extraction of the reduced cross section

17.1 Data and theory matching

From the PWIA, we know that we can factorize the differential cross section depending on the spectral function via the following equation:

$$\frac{d\sigma}{dE_{e'}dE_p d\Omega_{e'} d\Omega_p} = K\sigma_{ep} S(E_m, p_m) \tag{11}$$

From the experimental data, we can extract the experimental cross section:

$$\frac{d\sigma}{dE_{e'}dE_p d\Omega_{e'} d\Omega_p} = \frac{N(E_m, p_m) - N_B(E_m, p_m)}{L \cdot T_p \cdot \epsilon \cdot \Phi(E_m, p_m)} \tag{12}$$

To get the true number of events, we have several efficiencies to take into account, proton transmission, dead time, detectors efficiencies, blocking efficiency[1] and the background subtraction based on the coincidence time.
Then the yield has to be divided by the phase space factor and corrected for the radiative effects.
The cross section is then calculated from the experimental inputs and then weighted by the charge, the efficiencies and the correction factors.

For the first extraction, we will get a radiated reduced cross section, using the following formula. It is based on an event by event calculation in order to calculate the cross section of the process, and then the various factors are included for the normalisation.

$$S(E_m, p_m) = \frac{1}{L \cdot T_p \cdot \epsilon \cdot \Phi(E_m, p_m)} \sum_{counts} \frac{1}{\sigma_{ep} E_{e'} p_{p'}} \tag{13}$$

17.2 Deradiation of the data

We can deradiate the data through an iterative process described in the following. The input is coming from the experimental radiated spectral function we calculated. It is used

---

[1] Blocked coincidences occur when a random singles trigger arrives just before a true coincidence event. This correction is in the worst case of the order of 2%.

by SIMC to generate the radiative correction factors, $C^{derad}(E_m, p_m)$.

$$C^{derad}(E_m, p_m) = \frac{N_{norad}(E_m, p_m)}{N_{rad}(E_m, p_m)} \tag{14}$$

We then extract a new spectral function corrected in first order for the radiative process. The strong influence of the Bremsstrahlung may be seen for some kinematics with more than 80% of radiated events. The procedure is redone until a fair agreement is found between simulation and data.

$$S(E_m, p_m) = \frac{1}{L \cdot T_p \cdot \Phi(E_m, p_m)} \sum_{counts} \frac{1}{\sigma_{ep} E_{e'} p_{p'}} C^{derad}(E_m, p_m) \tag{15}$$

17.2.1 Deradiation of an IPSM yield

By generating with SIMC a yield based on the IPSM model that is usually used, and by applying our extraction procedure to it, we can easily check if we get back the theoretical input. It may also be seen as an estimate of the precision we can reach with this kind of procedure. The result is shown in figure 34. We can state a good agreement between both. We notice that a part of the strength originating from the first shell is shifted to the other shell due to the width of the shells that are different and the simple integration made only on one energy region.

17.2.2 Application to the quasielastic data

For the quasielastic data, we already mentioned the good agreement between the data and simulated yields. We therefore just apply a first order extraction of the spectral function. As we did not iterate the process other times, we will still get an influence from the radiative processes. Moreover the influence of other processes as SRC or FSI prevent to get the IPSM input. Nevertheless, the reconstructed shells of carbon with a very simple cut on the energy regions are in a correct agreement with the IPSM model(figure 34).

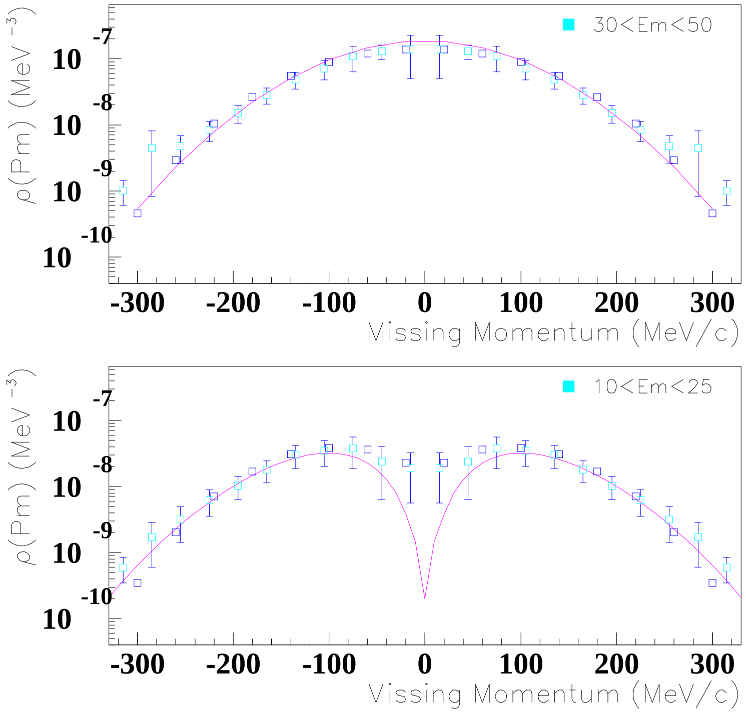

Figure 34: Shell momentum distribution for carbon. The light blue squares stand for the extracted values from the experimental data, the blue squares correspond to the extracted simulated yield, and the magenta line corresponds to the IPSM input spectral function.

18 Results for Carbon

18.1 Comparison with the simulation

By its purpose this experiment goes further than the usual spectral function studies. First we extract the deradiated spectral function in order to observe the influence of the SRC and then take a further step in handling the FSI/MSP.

We can compare several spectra of simulation and data, for the momenta, the angles, the missing momentum and missing energy. The good reproduction of one of these variables doesn't mean that all of them are correctly reproduced by the re-iterated spectral function. We control the iterative process with the quality of the agreement of the reproduced spectra to the data. To avoid the fact that even with a bad agreement, the process is already given its best fit, we use a one and two-step differences between the obtained spectral function to check that the discrepancy between two iterations is smaller than 0.5%. This last point is used to get an idea of the convergence of the process.

Two different bin sizes are used in the analysis for E_m, most often we used a width of 20 MeV, but in some case, we also use 40 MeV. The bin size for p_m has always the same value of 40 MeV/c.

The results for the production runs for carbon in parallel kinematics are different from perpendicular kinematics where one cannot use any suppression of the Δ resonance excitation. For the parallel kinematics it is possible to use a kinematical cut on the missing momentum and angle to separate quasielastic and Δ events.

This pion cut is to be considered in two parts, first a region below 150 MeV where the energy is too small for producing a pion, and the one above where one can distinguish two regions in the plane p_m/θ. The transverse character of the delta resonance leads to angles between particles that tend to be bigger than the ones for quasielastic events (as shown in figures 42 and 43).

From these kinematical restrictions, we are able to constrain the correlated region we want to investigate. First we deal with energies larger than 60 MeV and lower than a limit corresponding to the rise of the Δ production. For the momenta, we choose to go from 230 MeV/c to a maximum of 650 MeV/c. This definition of a good correlated region inside the kinematics availability is used in order to compare with calculations from Benhar and to set limits to extract the momentum distributions and the integrated strengths for the different targets and kinematics.

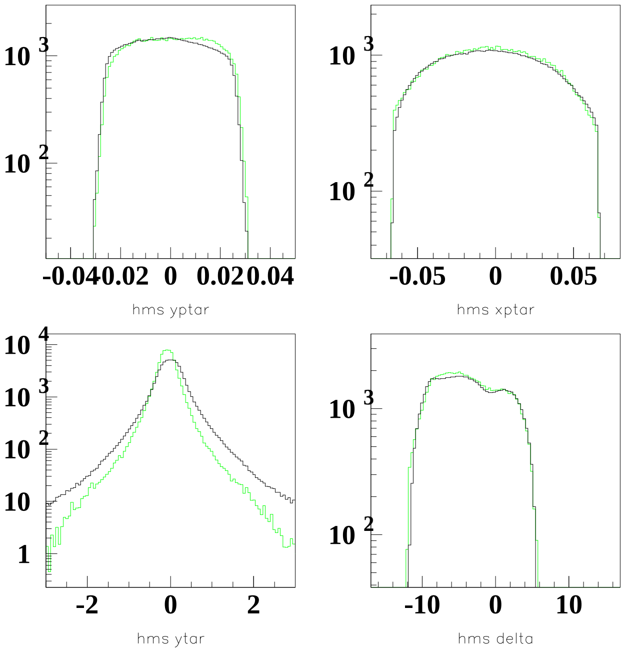

Figure 35: HMS spectrometer variables. The green histograms correspond to the simulation and the black ones to the data from kinematics 5.

18.2 Results for Perpendicular kinematics

18.2.1 Comparison data-Monte-Carlo

We have a fair agreement between input spectral function and radiated spectral function after only a few iterations. As shown in figures 36 and 37, the SOS and HMS quantities are well reproduced and the same is true for the missing energy and missing momentum spectra. It is known on the other hand that the contamination by the delta and rescattering processes is quite high. The extracted spectral function is then to be considered as deradiated but contaminated.

18.2.2 Spectral function in perpendicular kinematics

The result is shown in figure 38. We notice the resonance region for E_m larger than 200 MeV.

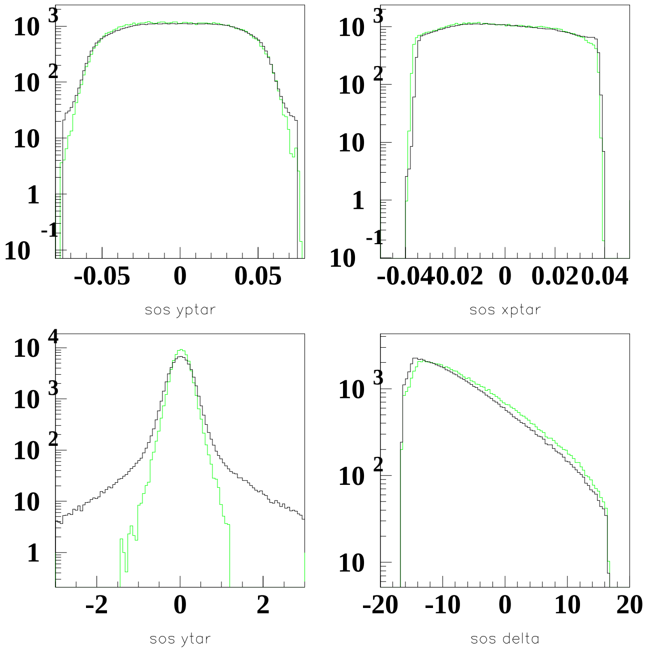

Figure 36: SOS spectrometer variables. The green histograms correspond to the simulation and the black ones to the data from kinematics 5.

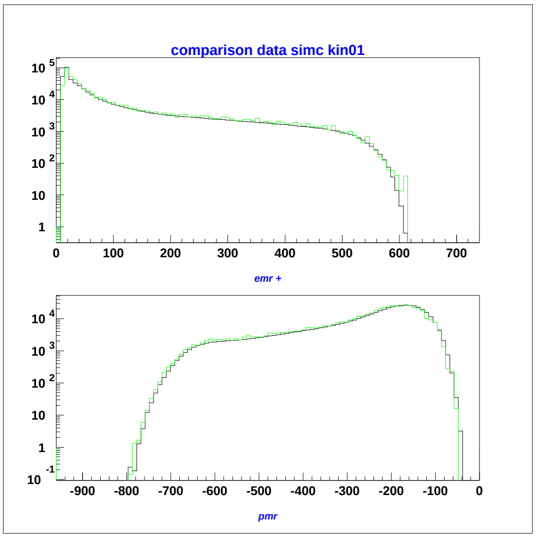

Figure 37: Missing energy and missing momentum for perpendicular kinematics p1. Data are in black and simulation in green.

18.3 Results in parallel kinematics

We will show two different results in this part, the first corresponds to the extraction of the parallel spectral function by applying the process to the whole E_m, p_m kinematical plane. The result is then directly compared with the one in perpendicular kinematics. Then we can also exploiting the transverse character of the Δ resonance, define a kinematical cut that gives access to a spectral function with a dramatic reduction of the Δ contribution. This cut is referred in the following as pion cut.

18.3.1 Spectral function in parallel kinematics

Here we also get a good agreement between the yields (figure 39). The resulting spectral function is shown in figure 40. We clearly see the resonance region, mainly the Δ, after the gap. It is also noticed that the extracted spectral function is smaller than the one in perpendicular kinematics for the same momentum bin. It is what was expected with an enhancement of the MSP in the perpendicular kinematics.

18.3.2 Corrected spectral function in parallel kinematics

By the use of the pion cut, we can separate in a very simple way the delta events from the real ones. By the use of the transverse feature of the Δ resonance, these events are

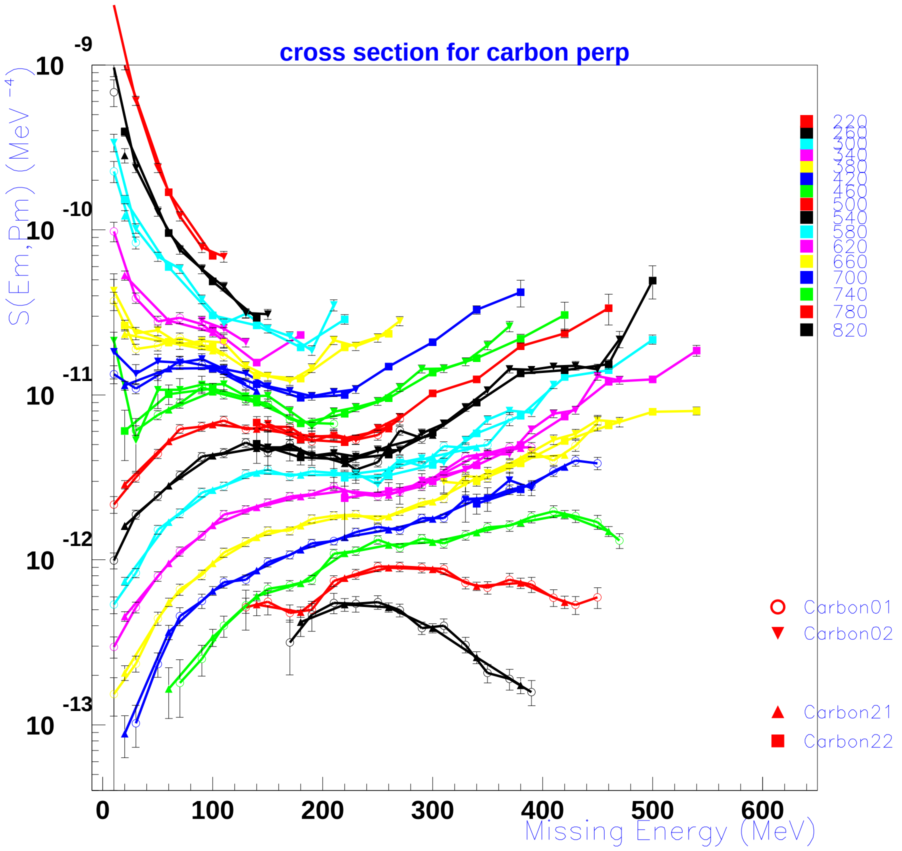

Figure 38: Spectral function for perpendicular kinematics. The two kinematics are shown. The data labeled with '21' and '22' correspond to the analysis with different bin size, 40 instead of 20 MeV for E_m, in order to avoid the lack of statistics in certain regions. Statistical errors only are included.

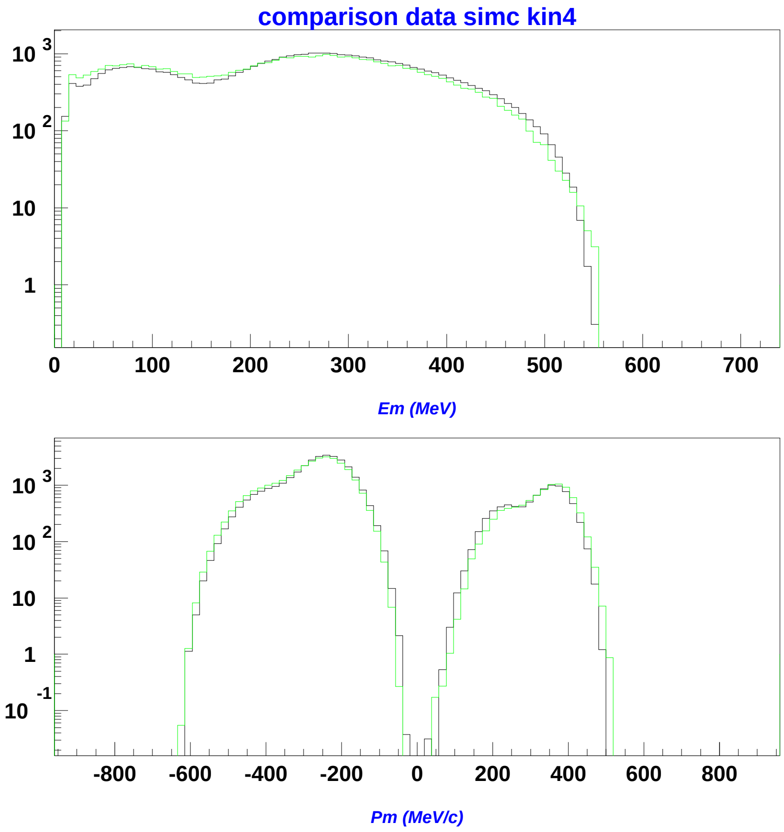

Figure 39: Missing energy and missing momentum for parallel kinematics 4. Data are in black and simulation in green.

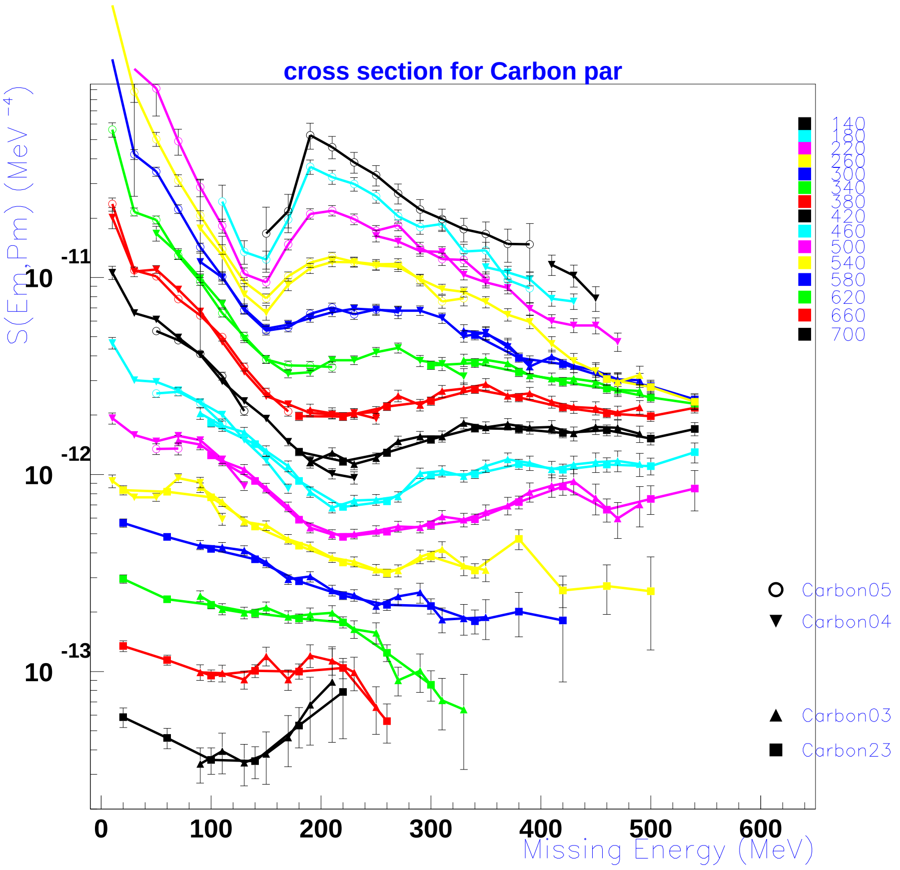

Figure 40: Deradiated spectral function for parallel kinematics. The data '23' correspond to the analysis for the kinematics 3 with different bin size of 40 instead of 20 MeV for E_m. Statistical errors only are shown.

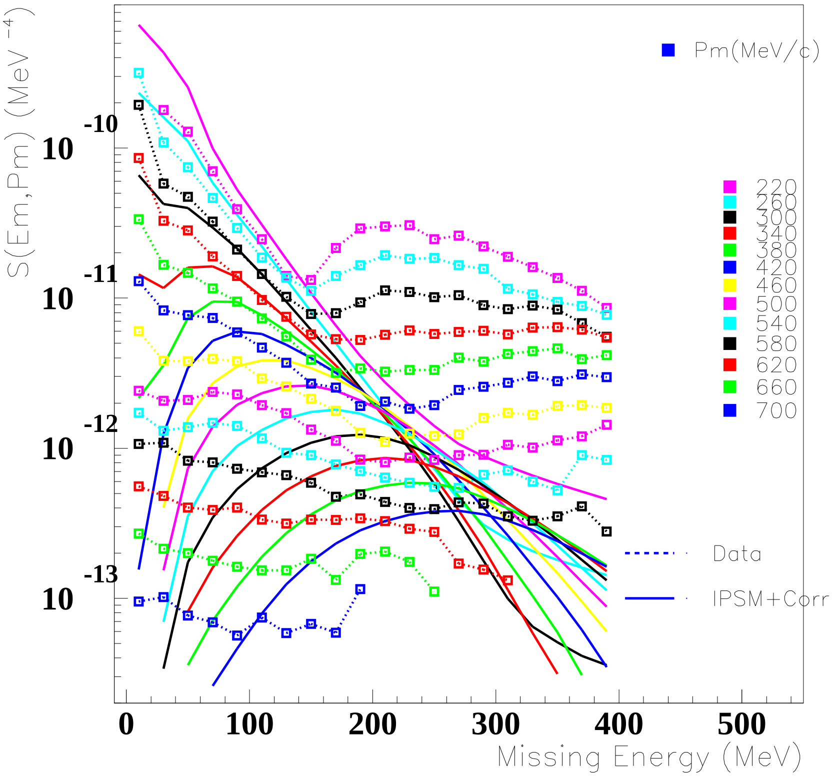

Figure 41: Deradiated spectral function for carbon in parallel kinematics, comparison with the model including the IPSM and the correlated part from Benhar.

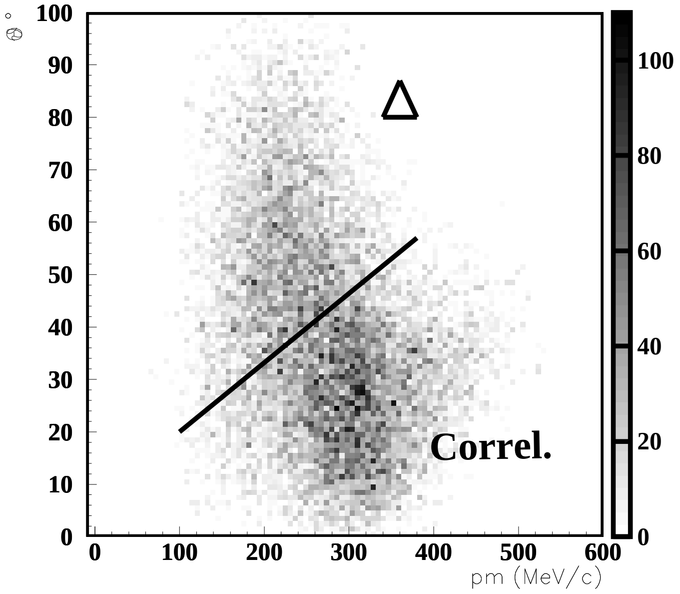

Figure 42: Plot of the momentum as function of the angle between particles for kinematics 5. The application of the pion cut (black line) allows to partially get rid off the resonance of the deltas.

more likely to show at bigger angles than the ones coming from the regular scattering. On figure 42, we can state that the events on the lower part are the good ones, whereas the events from the upper region are mainly Δ. It is obvious that this kind of cut is not as good as the separation one is able to achieve for the hydrogen data(cut on the invariant mass) but it does allow a better look at the correlated region.

18.4 Momentum and energy distributions

We integrated the spectral function one time to get the momentum distribution, and a second time to obtain the integrated strength. For the E_m integration, we choose the upper limit at the gap between the two regions in order to avoid as far as possible the Δ contamination.

$$n(P_m) = \int_{60}^{\Delta_{lim}} dE_m \cdot S(E_m, P_m) \tag{16}$$

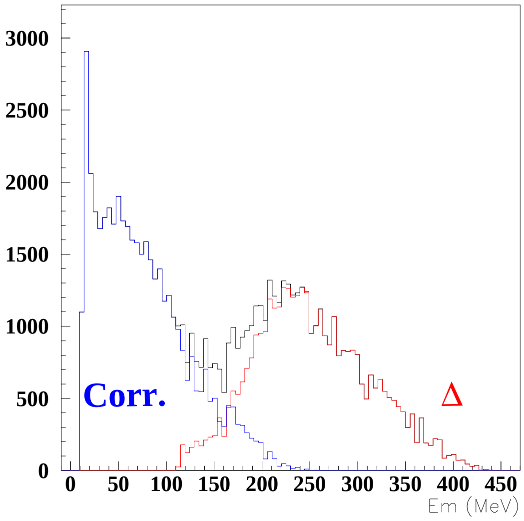

Figure 43: Plot of the missing energy using the pion cut. The blue histogram corresponds to the part that contains the correlation yield and the green to the resonance of the deltas.

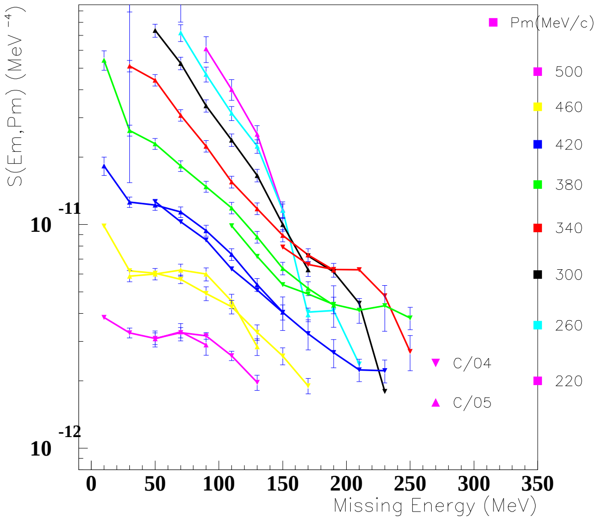

Figure 44: Deradiated spectral function for parallel kinematics, with the use of the kinematical pion cut.

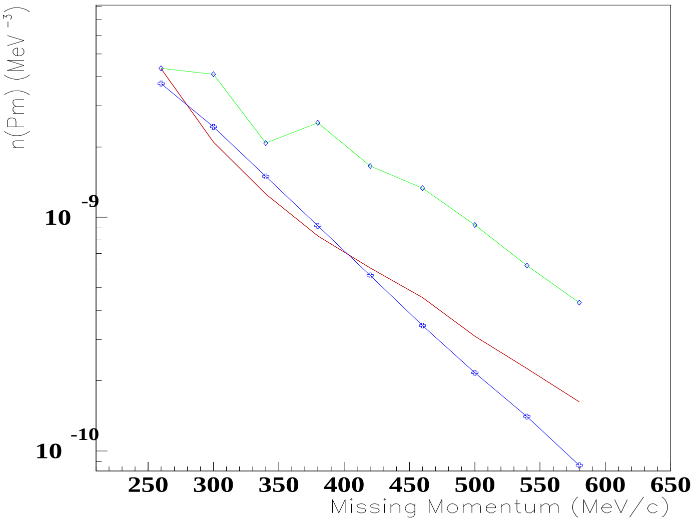

Figure 45: Momentum distribution for perpendicular and parallel kinematics. The green curve corresponds to the perpendicular kinematics, the blue corresponds to the parallel kinematics, and the red curve corresponds to the one extracted from calculations.

$$Z_{Corr} = 4\pi \int_{230}^{650} dP_m \cdot {p_m}^2 \cdot n_{exp}(P_m) \tag{17}$$

We obtain the results shown in 45. Here we easily see that the yield measured in the perpendicular kinematics is much bigger than in the parallel kinematics. The integrated strengths obtained are even more eloquent. Indeed, the integrated strength is 0.549 for the parallel kinematics and 1.265 for the perpendicular one. From this result we can deduce two facts. First, the contribution of FSI in this region may be as much as the double of our signal in perpendicular kinematics. Secondly, that in parallel kinematics where we have minimized the effects of FSI, we find only 9% of the total strength; the rest is spread over other kinematical regions not covered here.

Even if the spectral function gets small for very high momenta, the integral is not insensitive to the upper limit. The choice of an upper limit of 630 MeV/c, gives 0.540 for parallel and 1.207 for perpendicular kinematics integrated strengths, that means roughly a 5% difference. The theory of Benhar, gives a theoretical integrated strength of 0.599 (resp. 0.577).

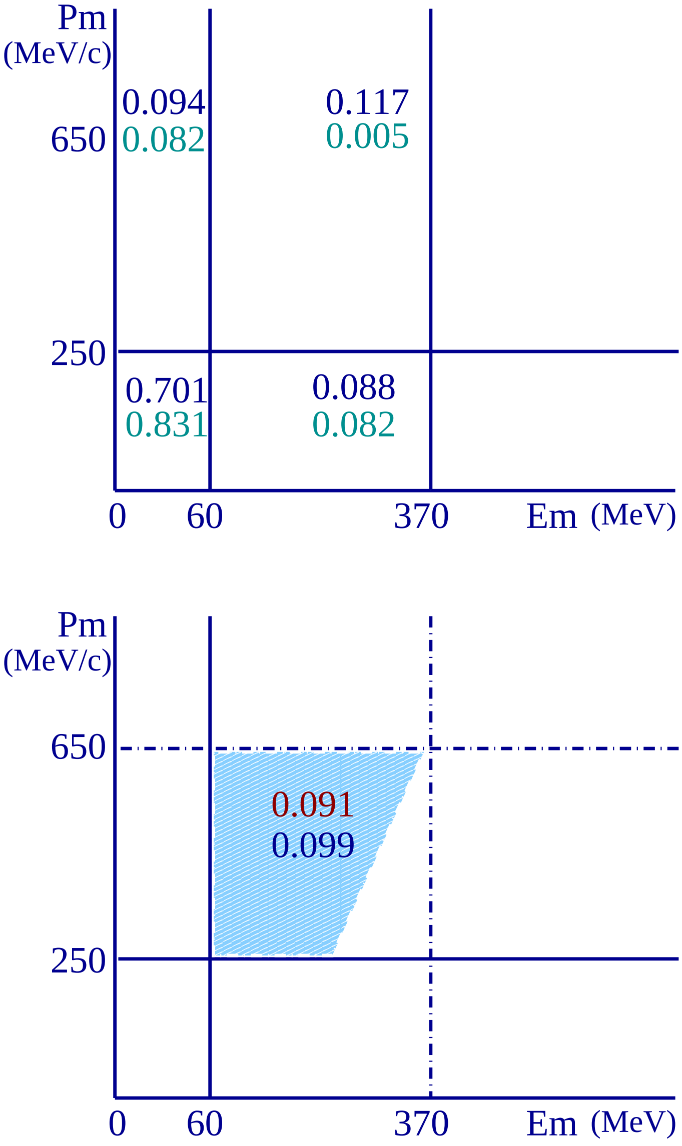

Figure 46: Comparison of the correlated strength distribution. On the first figure are shown the values related to the whole strength coming from the CBF theory (in dark blue) and the IPSM model (in green). On the second figure, the result in blue corresponds to the CBF theory value and the one in green corresponds to the experimental value for the accessible region in momentum and energy depicted in light blue.

19 Results for the aluminium target

19.1 Results for perpendicular kinematics

This target shows the same behavior as carbon. The modus operandi is the same as the one used for carbon. The same kinematical cuts were also applied. The same restrictions and regions are considered.
As the number of nucleons is not far from one of carbon, we expect that the behavior is very close too. Especially because the strength originating from N-N interaction should be independent of the nucleus size, the correlated part must be the same, only the influence of FSI, and in particular MSP is supposed to be bigger.

19.1.1 Comparison data/Monte Carlo

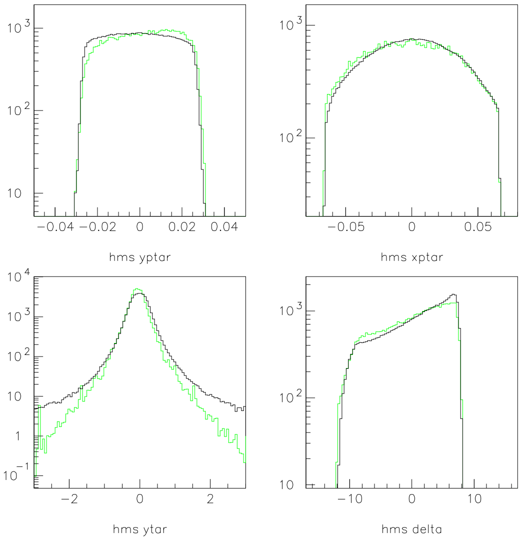

Figure 47: HMS spectrometer variables. The green histograms correspond to the simulation. The black histograms correspond to the data. The plots correspond to kinematics p1.

19.1.2 Spectral function in perpendicular kinematics

This target, as the carbon target, shows for the perpendicular kinematics a poor separation between the region dominated by the Δ resonance and the one dominated by

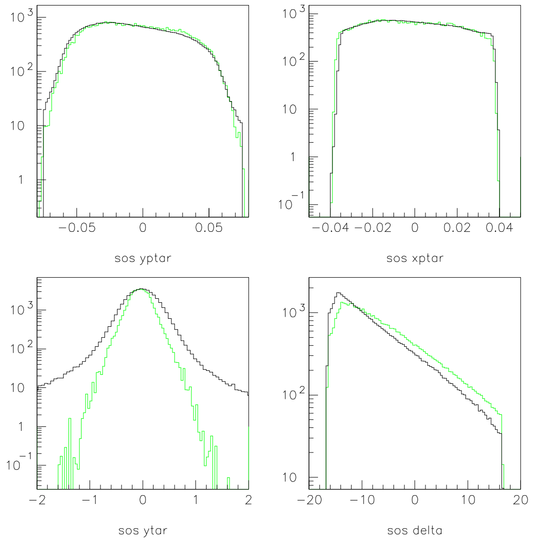

Figure 48: SOS spectrometer variables. The green histograms correspond to the simulation. The black histograms correspond to the data. The plots correspond to kinematics p1.

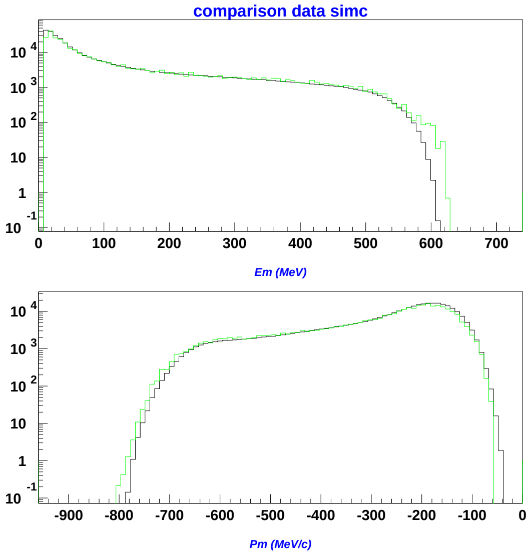

Figure 49: Missing energy and missing momentum for kinematics p2. Data are in black and simulation in green.

the correlations. We can guess for momenta in a range from 420 to 540 MeV/c that for energies bigger than 220 MeV, the process is dominated by the Δ contribution.

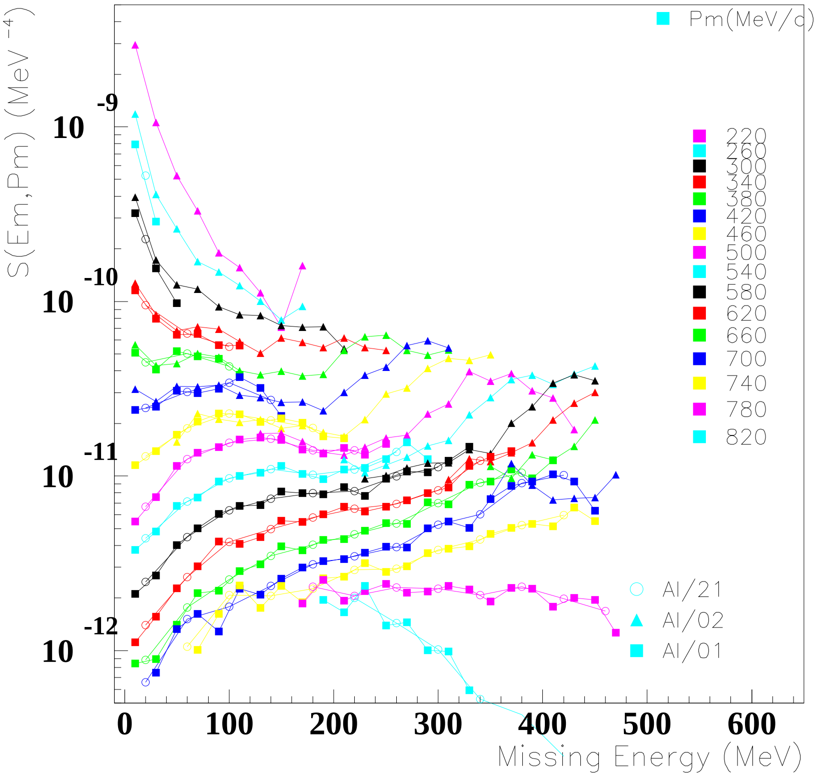

Figure 50: Spectral function for Aluminium in perpendicular kinematics p1 and p2. The data indicated as 21 correspond to the kinematics p1 analysed with a bin size of 40 MeV instead of 20 MeV for 01.

19.2 Results for parallel kinematics

This target shows the same behavior than carbon. The modus operandi is the same than the one used for carbon. The same kinematical cuts were also applied. The same restrictions and regions are considered.

19.2.1 Spectral function in parallel kinematics

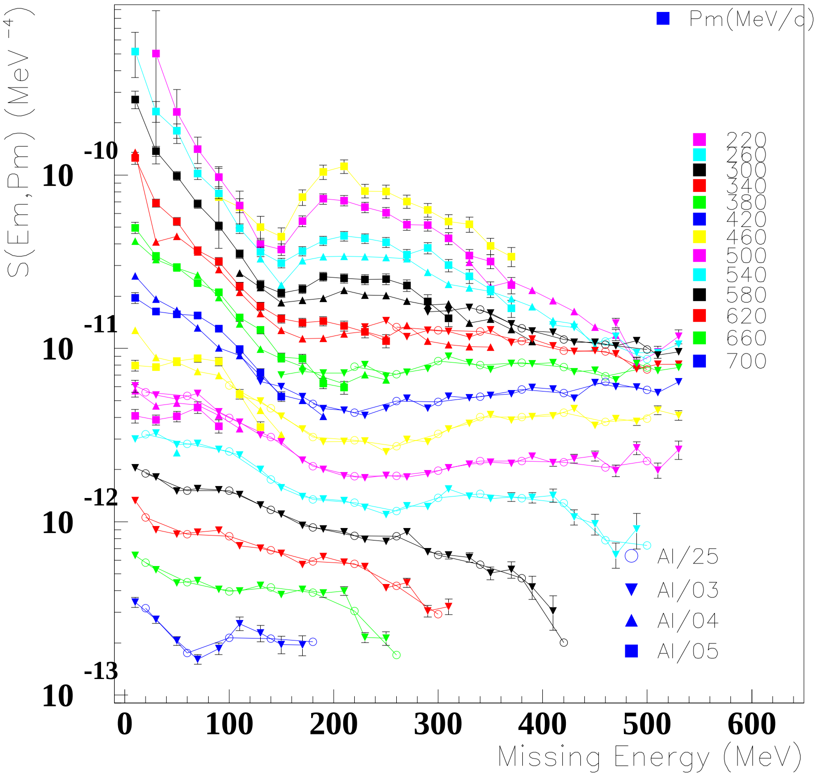

Figure 51: Spectral function for Aluminium in parallel kinematics 3, 4 and 5. The data indicated as 25 correspond to the kinematics p1 analysed with a bin size of 40 MeV instead of 20 MeV for 05.

20 Results for the iron target

The background contribution, as well as the effects of MSP are stronger for this heavy target. The behavior is nevertheless roughly the same as for carbon and aluminium (see figures 52, 53).

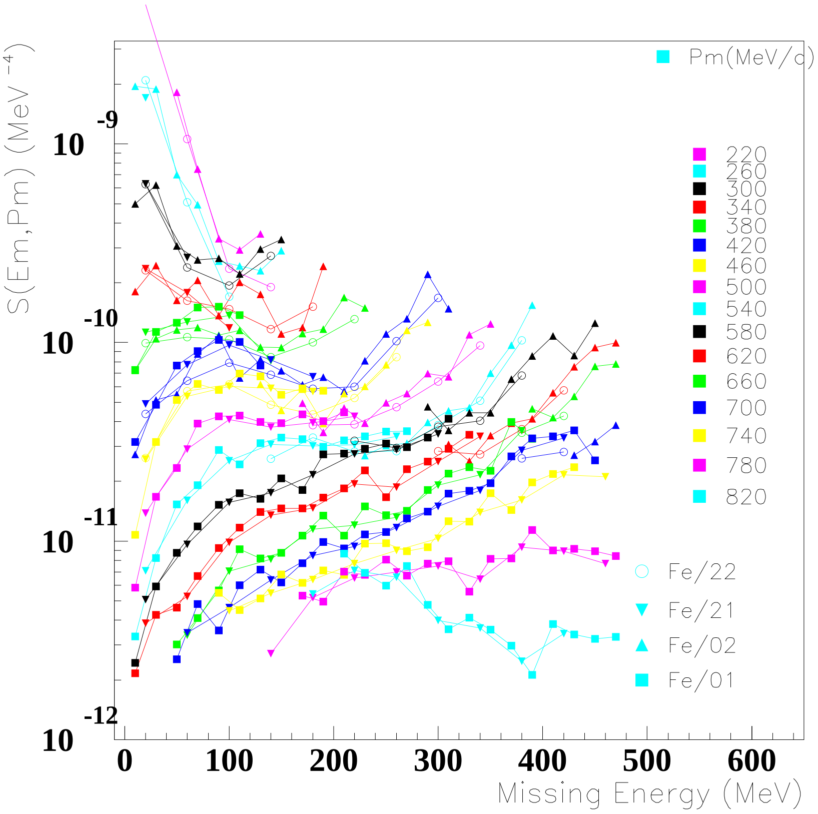

Figure 52: Spectral function for Iron in perpendicular kinematics p1 and p2.

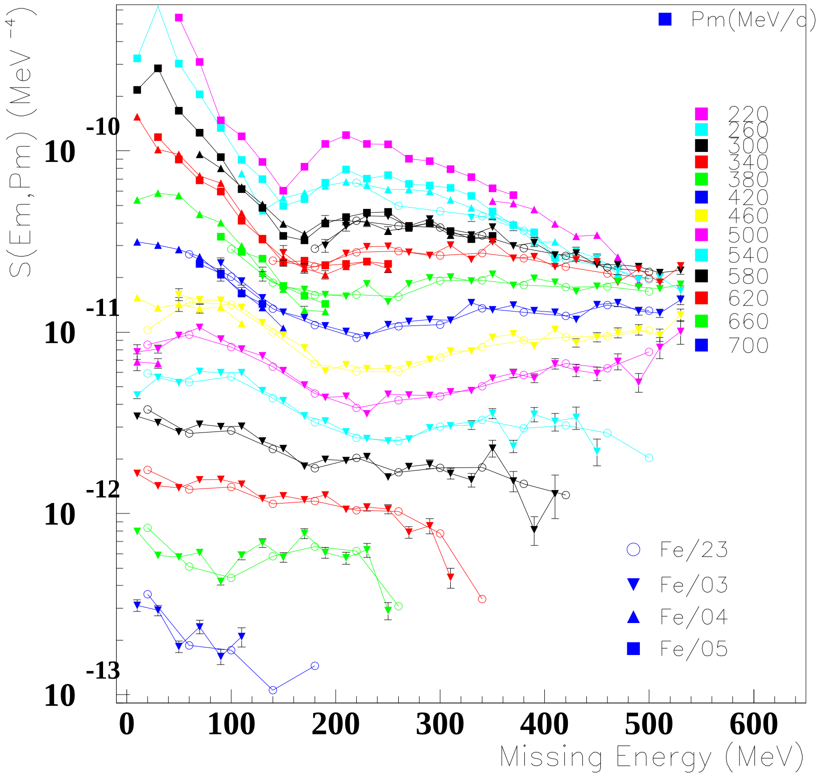

Figure 53: Spectral function for Iron in in parallel kinematics 3, 4 and 5.

21 Results for the gold target

The background contribution, as well as the effects of MSP are stronger for this heavy target(see figures 54, 55). In figure 56, the comparison with the calculations from Benhar shows large excess of strength even for the parallel kinematics.

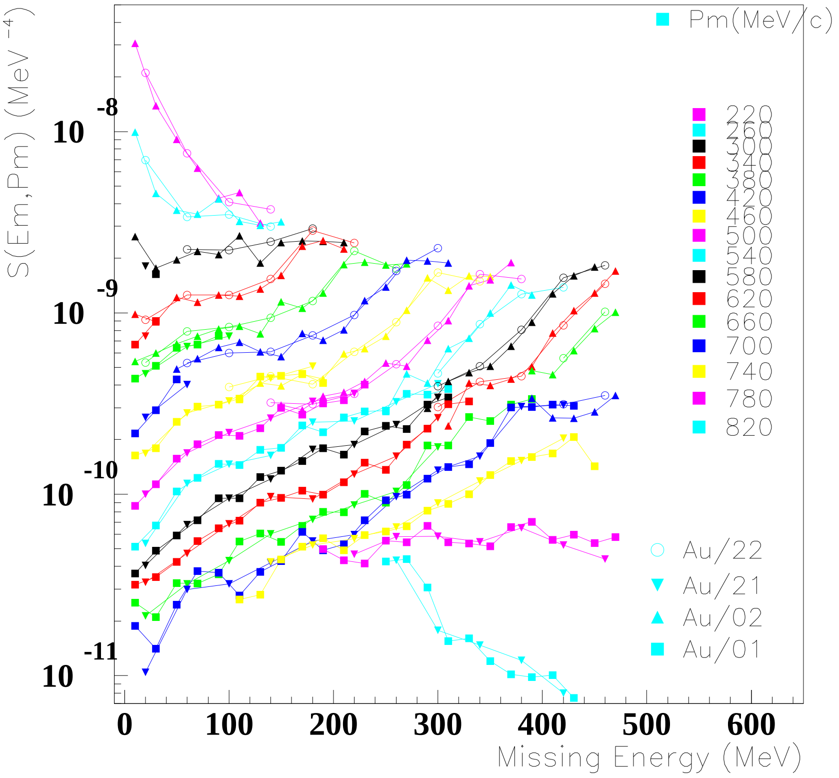

Figure 54: Spectral function for Gold in perpendicular kinematics p1 and p2.

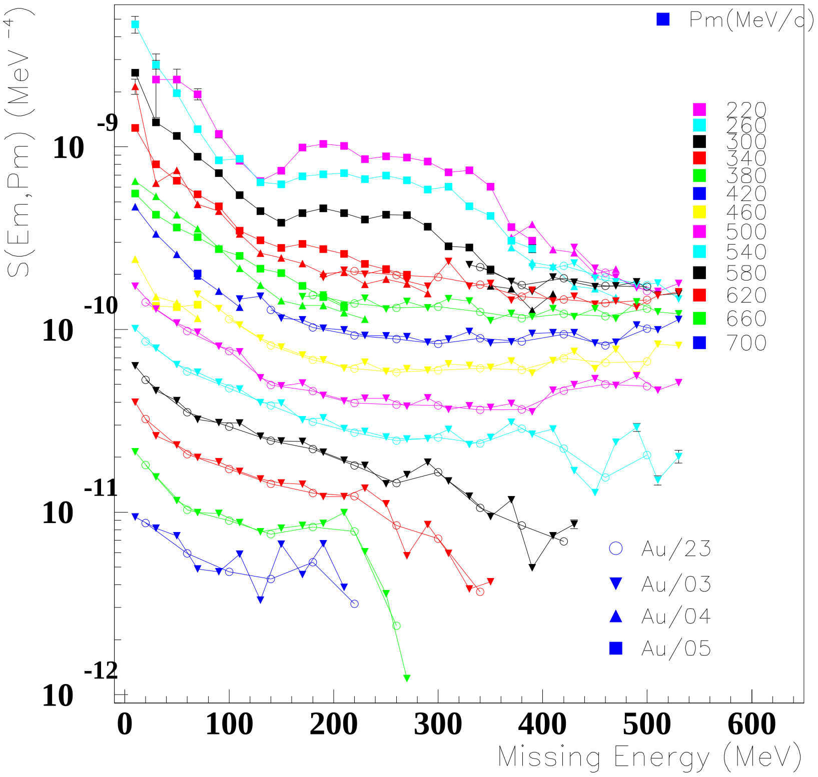

Figure 55: Spectral function for Gold in in parallel kinematics 3, 4 and 5.

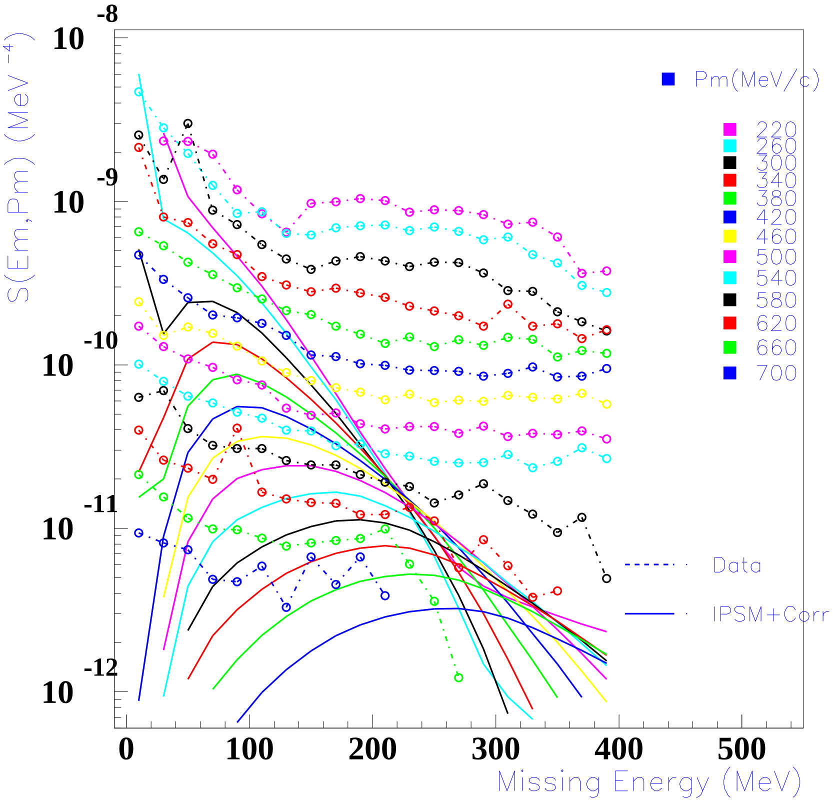

Figure 56: Spectral function for Gold in parallel kinematics compared with the model including the IPSM part and the correlated part from Benhar.

21.1 Comparison between targets

We clearly see that we got a good agreement between the scaled spectral function for the different targets except gold. The rescattering process and the coulomb corrections are believed to be more important for this heavy nucleus, and this may affect dramatically our yield. Some recent calculations from Barbieri, [24] give indication for the importance of rescattering.

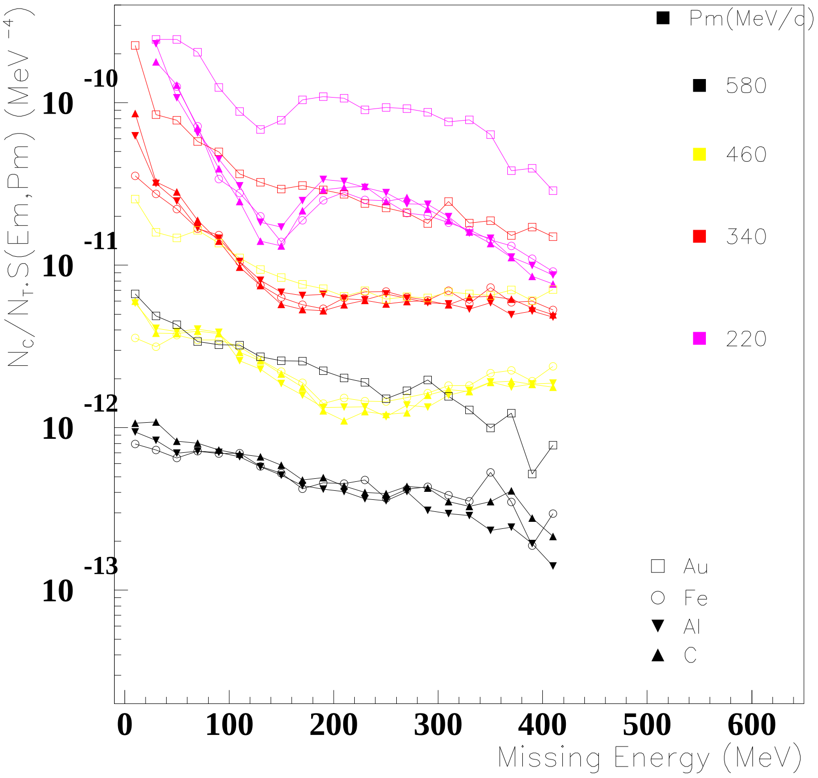

Figure 57: Spectral function for the different targets in parallel kinematics. The spectral function is normalised to carbon according to the number of protons inside the nucleus.

22 Systematics

Various error sources have to be taken into account for the extraction of the experimental spectral function. Some sources, such as the radiative corrections, are also taken in account in the statistical ones.

22.1 Systematic errors from the experiment

Several uncertainty sources originate from the experimental setup. The beam, the target and the spectrometers contribute to them.

Item	% of uncertainties in data yield
Current measurement	1. / 2.
Solid target thickness	0.1
HMS tracking efficiency	1.
SOS tracking efficiency	1.
Proton absorption	0.5
Background subtraction	0.3
Constraints stability	1.
Beam and spectrometer offsets	1.
Sum in quadrature	2.3 / 2.9

Table 9: Experiment dependent uncertainties.

22.2 Systematic errors from the model

We use several inputs from the Monte Carlo simulation in our analysis process. Some quantities that we calculate are sensitive to changes in the procedure. The off-shell cross section uncertainty is estimated by running our code with the σ_{CC1} and the σ_{CC2} prescriptions from DeForest [15]. The analysis is done with the σ_{CC1} prescription, the difference to the analysis using σ_{CC2} is around 10 %(see appendix B) .

As discussed earlier, the value chosen for the transparency is given in the table 8. From the previous experiments made, as shown in figure 33, we assign an uncertainty of 10 % to this quantity.

Item	% of uncertainties in simulated yield
DeForest prescription	10.
Nuclear transparency	10.
Internal Bremstrahlung External Bremstrahlung	2. 2.
Sum in quadrature	14.4

Table 10: Model dependent uncertainties.

Part IV

Conclusions

We used the experimental approach described in this thesis to determine the strength of the spectral function where few data is available. For the different nuclei investigated, it shows a similar behavior for the region that is not dominated too much by the FSI. Except for the gold target, the spectral function scales with the number of protons inside the nucleus, as it is expected from processes related to short range correlations. The comparison with the calculations from Benhar shows an important difference with the data taken in perpendicular kinematics, while the agreement with the data taken in parallel kinematics is better, in particular the "correlated number of protons" is roughly the same. Concerning this "correlated number of protons", we found in the studied region a number that corresponds to 10% of the total number of protons of the nucleus. The expected value from the protons affected by the short range correlations is believed to be of the order of 15-20 %, the difference between these two values is coming from the fact that we do not probe the whole correlated region. Short range correlations have also an effect in the regions of small energy and small momenta.

We also see from the different targets and from the strength difference between parallel and perpendicular kinematics that FSI are as important as thought for perpendicular kinematics, and that these processes may overwhelm completely the signal due to correlations. New calculations performed by Barbieri [24] are also confirming this fact.

The strong interest for the short range part of the nucleon-nucleon interaction is obvious when one looks at the different reviews and experimental proposals concerning this topic. The possibility to handle the competing processes with a judicious choice of kinematics allows to extract via the spectral function a signature beyond the IPSM. The agreement with the calculations of Benhar in parallel kinematics, the scaling for the different nuclei, together with the minimisation of the FSI, make us identify this enhancement of the spectral function as a clear experimental signature of short range correlations.

If some work is still required to get a good theoretical description of the whole reaction, especially concerning the FSI, this experiment gives milestones for further investigations.

References

[1] U. Amaldi, *et al, Phys. Rev. Lett. 13:341*, 1964.

[2] V. Pandharipande, I. Sick, PKA de Witt Huberts, *Rev. Mod. Phys. 69:981* , 1997.

[3] O. Benhar *Nucl. Phys. A505:267*, 1989.

[4] I. Sick, S. Fantoni, A. Fabrocini, O. Benhar, *Phys. Lett. B323:267*, 1994.

[5] D. Van Westrum *Quasielastic (e,e'p) Reactions and Proton Propagation through Nuclei*, PhD Thesis, University of Colorado, 1998.

[6] D. Dutta *The (e,e'p) Reaction Mechanism in the Quasi-Elastic Region*, PhD Thesis, Evanston, Illinois, 1999.

[7] D. Dutta *Radiative corrections for Jlab experiments*, HallC documentation.

[8] J. Arrington *A-B-SIMC*, HallC documentation.

[9] J. Arrington, PhD thesis, Caltech, 1998.

[10] N.C.R. Makins, PhD thesis, MIT, 1994.

[11] J. Volmer, *The Pion Charge Form Factor via Pion Electroproduction on the Proton*, PhD Thesis, Vrije University, 2000.

[12] I. Sick, *Correlated Spectral Function and (e,e'p) reaction mechanism, TJNAF proposal, June 1997.*

[13] T. Frick, *et al.*, *arXiv:nucl-th/0406010*, 2004.

[14] J.A. Templon, *Fizika B8:117*, 1999.

[15] T. DeForest, *Nucl. Phys., A392:232*, 1983.

[16] P. Mergell, Ulf-G. Meissner, D. Drechsel, *Nucl. Phys. A596:367*, 1996.

[17] J.A. Templon, C.E. Vellidis, R.E.J. Florizone, A.J. Sarty, *Phys. Rev. C 61 014607*, 2000.

[18] S. Stein, W.B. Atwood, E.D. Bloom, R.L.A. Cottrell, H. DeStaebler, C.L. Jordan, H.G. Piel, C.Y. Prescott, R. Siemann, and R.E. Taylor. *Phys. Rev. D., 12:1884, 1975.*

[19] L.W. Mo and Y.S. Tsai. *Rev. Mod. Phys., 46:815, 1969.*

[20] Y.S. Tsai. *SLAC Report, SLAC-PUB-848, 1971.*

[21] D.Dutta, D. Van Westrum *et al.*, *Phys. Rev. C 68 064603*, 2003.

[22] K. Garrow, *Phys. Rev. C 66, 044613*, 2002.

[23] T.G. O'Neill, PhD thesis, Caltech, 1994.

[24] C. Barbieri, *Proc. 6th workshop on e-m induced two-hadron emission, Pavia*, 2003.

[25] D. Rohe, *Proc. 6th workshop on e-m induced two-hadron emission, Pavia*, 2003.

[26] D. Rohe, *Correlated Strength in Nuclear Spectral Function* submitted to Phys. Rev. Lett.

A Energy measurement

As mentioned in the experiment part, the energy is measured using the superharps in the Hall C arc(P. Gueye). The table is giving the results for the experiment time.

Date	Energy
Aug. 18th	3297,183±0.808 MeV/c
Aug. 20th	3296,573±0.810 MeV/c
Sep. 27th	3121,953±0.767 MeV/c
Oct. 5th	3118,696±0.764 MeV/c

Table 11: Beam Energy measurements.

B De Forest cross sections

To calculate the cross sections for electron scattering on a bound (off-shell) nucleon, various approximations and assumptions are made resulting in several off-shell cross section prescriptions. The most widely used are the off-shell prescriptions σ_{cc1} and σ_{cc2} from DeForest [15].

The subscript cc is for current conservation and refers to the fact that current conservation $\overrightarrow{q}.\overrightarrow{J} = \omega\rho$ is restored. This is done by using this relation to eliminate the longitudinal component of the current.

We use in the analysis the σ_{cc1}, but as a test to check the uncertainty to be assigned to this quantity, we performed the analysis also with σ_{cc2}. The results are shown in figure 58. We notice that for the correlated region the difference between the two curves stays in the limit of 10/12 %, but in the Δ region this difference increases.

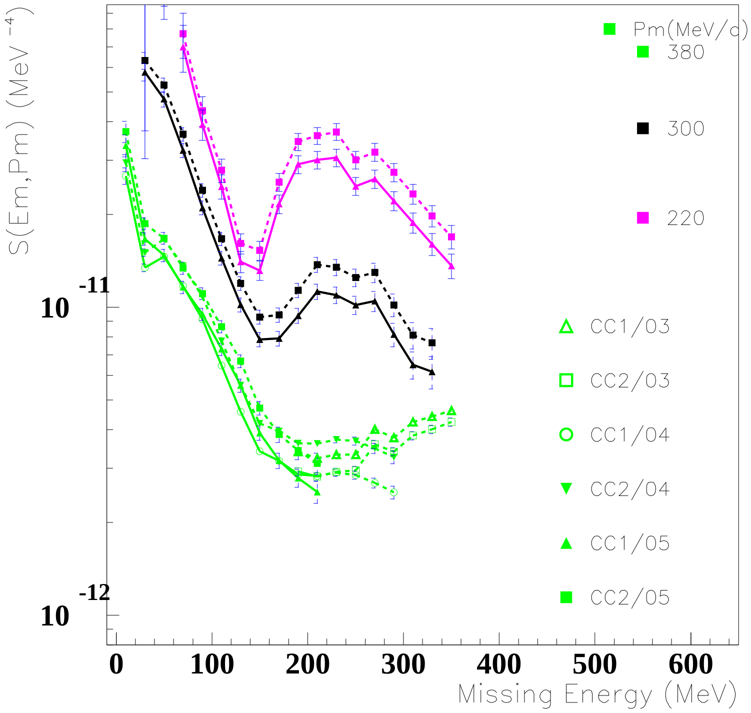

Figure 58: Comparison of the carbon spectral function using σ_{cc1} and σ_{cc2} prescriptions from deForest.

Curriculum Vitae

Données personnelles:

Nom: Christophe Normand
Date de naissance: 02 Février 1973
Lieu de naissance: Bordeaux, Gironde, France.
Nationalité: Française
Adresse: 28 rue du Ventron, 68100 Mulhouse

Formation:

1994-1997: Ecole Nationale Supérieure d'Ingénieur de Strasbourg,
Université Louis Pasteur,
Diplôme d'ingénieur option physique,
Diplôme d'Etude Approfondies en Physique Subatomique.
1991-1994: Lycée Camille Jullian, Bordeaux,
Classes préparatoires Mathématiques.
1990-1991: Lycée Charles Secondat de Montesquieu, Bordeaux,
Baccalauréat série C, mention bien.

Activités scientifiques:

Depuis 1999 Participation aux expériences du groupe du Professeur Sick
Jefferson Laboratory, Virginia, MAMI, Mainz, PSI, Villigen.
1997 Laboratoire SUBATECH, Nantes,
Travail sur des formules analytiques sur les processus de fusion et fission nucléaires.

Publications:

G. Warren *et al.*, Measurement of the Electric Form Factor of the neutron at Q2 =0.5 and 1.0 GeV2 /c2. , *Phys. Rev. Lett. 92 (2004) 042301.*
J. Bermuth *et al.*, The neutron charge form factor and target analyzing power from 3He(e,e'n) scattering , *Phys. Lett.B564 (2003) 199.*
C. Carasco *et al.*, Final state interaction effects in polarized 3He(e,e'n), *Phys. Lett.B559 (2003) 41.*
G. Kubon *et al.*, Precise neutron magnetic form factors, *Phys. Lett.B524 (2002) 26.*
G. Royer, C. Normand, E. Druet, Analytic description of the fusion and fission processes through compact quasimolecular shape, *Nucl. Phys. A634 (1998) 267.*